energies

MDPI

Article

Robust Sensorless Nonlinear MPC for PMSG-Based Wind Energy Conversion Systems with Three-Level NPC Converters

Abdelmoghit Fathelkhair [1], Hassan Abouobaida [2], Mohamed Nabil Srifi [2], Ahmed S. Alsafran [3,*], Abdullah A. Algethami [4], Habib Kraiem [5], Safeer Ullah [6], Khalid Faitah [1] and Younes Abouelmahjoub [1]

[1] LabSIPE, National School of Applied Sciences, Chouaib Doukkali University, El Jadida 24000, Morocco; fathelkhair123@gmail.com (A.F.); k.faitah@uca.ma (K.F.); younesprofagrege@gmail.com (Y.A.)
[2] Advanced Systems Engineering Laboratory, National School of Applied Sciences, Ibn Tofail University, Kénitra 14000, Morocco; abouobaida.hassan@uit.ac.ma (H.A.); srifimn@uit.ac.ma (M.N.S.)
[3] Department of Electrical Engineering, College of Engineering, King Faisal University, Al-Ahsa 31982, Saudi Arabia
[4] Department of Mechanical Engineering, College of Engineering, Taif University, Taif 21944, Saudi Arabia; a_algethami@tu.edu.sa
[5] Department of Electrical Engineering, Northern Border University, Arar 73213, Saudi Arabia; alhabeeb.kareem@nbu.edu.sa
[6] Department of Electrical Engineering, Quaid-e-Azam College of Engineering & Technology, Sahiwal 57000, Pakistan; dr_safeer_ullah@quaideazam.edu.pk
* Correspondence: aalsafran@kfu.edu.sa

Abstract

This paper proposes a computationally efficient sensorless control framework for a permanent magnet synchronous generator (PMSG)-based wind energy conversion system (WECS) employing three-level neutral-point-clamped (3L-NPC) back-to-back converters. A high-gain observer is developed to estimate grid voltages, frequency, and electrical angle, with its estimation error analyzed using Lyapunov theory to establish uniform ultimate boundedness. An integral sliding mode control (ISMC) combined with finite-control-set model-predictive control (FCS-MPC) is employed to regulate the system. To reduce the computational burden, a two-stage search algorithm is proposed, reducing the number of evaluated switching combinations from 27 to 7 per sampling period while maintaining comparable control performance. The proposed strategy is evaluated through Processor-in-the-Loop (PIL) simulations using MATLAB/Simulink and the LAUNCHXL-F28379D DSP platform. The observer is tested under sudden variations in grid voltage amplitude, abrupt frequency changes, frequency ramps, and measurement noise. The results show that the estimated variables converge toward their actual values, with increased fluctuations under measurement noise. The control strategy is evaluated under wind-speed variations and parametric uncertainties with a stochastic wind profile. Under nominal conditions, both FCS-MPC methods show comparable control performance, while the proposed method requires less execution time. Under parametric uncertainties, the proposed method improves DC-link voltage regulation and neutral-point voltage balancing, achieving a grid-current THD of 0.99%, compared with 2.43% for conventional FCS-MPC.

Keywords: integral sliding mode control; finite control set model predictive control; high-gain observer; processor-in-the-loop (PIL)

Academic Editor: Ramon Leyva

Received: 4 October 2026
Revised: 31 October 2026
Accepted: 6 November 2026
Published: 9 November 2026

Copyright: © 2026 by the authors. Licensee MDPI, Basel, Switzerland. This article is an open access article distributed under the terms and conditions of the Creative Commons Attribution (CC BY) license.

1. Introduction

Over the past few years, electricity has become the most widely used energy source globally, owing to its cleanliness and efficiency. In this context, the production of electrical energy has experienced significant development and represents a crucial area of research aimed at identifying suitable resources. Electricity producers have turned to renewable energy sources. Wind energy represents a promising and more cost-effective source, accounting for a significant share of the electricity generated from renewable energy sources [1]. The variation in wind energy production makes the development of wind energy conversion systems (WECSs) an appealing area of scientific research aimed at maximizing and adapting the extracted power to meet usage needs [2].

The capacity of installed wind turbines has seen a significant increase, requiring large-diameter turbines operating at low rotational speeds to minimize mechanical stresses related to design and implementation. The permanent magnet synchronous generator (PMSG) offers beneficial characteristics in terms of energy efficiency, self-excitation, control flexibility, reliability, ease of maintenance, and direct operation at low speeds, making the PMSG a favorable choice for high-power wind turbines. The use of power converters is essential. There are two types of configurations: the direct configuration, which uses a single AC/AC converter, and the indirect configuration, which uses two or more converters. The back-to-back topology with multilevel converters presents a promising solution for PMSG-based WECS, offering better performance in terms of total harmonic distortion (THD) and conversion efficiency. However, increasing the number of voltage levels requires more electronic devices and makes system control more complex. The back-to-back configuration with a three-level neutral-point-clamped (3L-NPC) converter remains an attractive choice, providing a good balance between energy quality, reduced switching losses, and DC-link voltage balance compared to the more complex five-level structure [3–5].

Several control techniques have been developed for WECSs, some employing modulators and others operating without them [6]. The PI controller is widely used for controlling wind systems. This controller generates the reference signal, which is then used by the modulator to produce the converter control signal. However, this modulation block adds an extra computational load. Other advanced control techniques have been developed for WECSs. In [7], a controller was designed based on fuzzy logic combined with a proportional–integral (PI) regulator, where the gains were optimized using interval Type-2 fuzzy logic. The developed regulator was tested under three-phase fault conditions and demonstrated the performance of the adopted strategy. However, the fuzzy logic technique requires a deep understanding of the system, a well-defined control rule base, and a significant number of tuning parameters, which can increase complexity and potentially affect control performance. Other control strategies have also been developed, including backstepping [8,9], adaptive control [10] and sliding mode control [11,12].

These control techniques operate with a fixed switching frequency and offer good stability and robustness. However, the continuous control laws generated must be converted into discrete switching states using the Pulse Width Modulation (PWM) method, which becomes more complex for multilevel converters [6,13]. Additionally, the neglect of constraints related to state variables and control inputs can sometimes result in control laws that are not feasible.

FCS-MPC is an appealing technique for dynamic system control and represents an important development avenue for controlling power converters that include the nonlinearity and limitations of electronic devices [14]. It is a discrete, direct, and nonlinear technique that addresses some of the drawbacks of indirect control methods. It offers several advantages, such as flexibility and simplicity in implementation on digital control boards, due to its discrete control criterion, which facilitates the transition from simulation models to practical realization. FCS-MPC eliminates the modulation step by directly selecting the combination to apply to the converter to minimize the cost function [15]. It executes a

https://doi.org/10.3390/en19215378

finite number of iterations, which depends on the topology being controlled. The cost function can include all system state variables to be optimized, with predefined constraints. It ensures better management of multivariable control independently, without the use of compensation terms, thanks to weighting coefficients [16].

However, the computational burden of FCS-MPC increases with the number of switching states considered in the optimization process. For a 3L-NPC converter, the conventional FCS-MPC evaluates 27 switching states during each sampling period, which can increase the computational requirements of the control system. Several research works on predictive control for WECSs have been published. In [17], a new control approach combining FCS-MPC and the Lyapunov function was developed to ensure the stability of the wind-power production chain during both standard and fault scenarios. The increase in DC-bus voltage is limited by using active energy storage through the inertia of the PMSG. However, the proposed method exhibits variable operating frequencies.

In [18], a nonlinear technique was used for the WECS with 2L-NPC back-to-back converters. The PI regulator and the SMC are used for the external loops on the machine side and the grid side, respectively, while predictive control is applied to the internal loops. The cost function minimization algorithm examines all possible combinations to determine the optimal switching state. The developed technique was validated both through simulation and experimentally. In [19], a new adaptive control strategy based on FCS-MPC for the back-to-back 3L-NPC conversion chain was proposed. The sliding mode technique is employed for the development of a load torque observer as well as the speed controller of the PMSG. The cost function minimization algorithm handles the 27 switching states to determine the optimal combination to apply to the converter, which increases the computational load.

To reduce this computational burden, Mayilsamy et al. [20] proposed a two-step cascaded cost function minimization algorithm based on virtual space vectors. The first phase aims to identify the sector, while the second phase determines the optimal combination, reducing the number of iterations compared with the conventional 27-state evaluation. However, the reference current on the machine side is provided by the optimal torque controller. In addition, these works rely on a set of sensors to measure the variables required for implementing the control strategies, which affects system reliability and increases its complexity. Therefore, reducing the number of evaluated switching states while reducing sensor dependency remains an important issue for the implementation of FCS-MPC in PMSG-based WECSs.

In this work, a WECS using a PMSG associated with two 3L-NPC converters interfaced with the electrical grid through an RL filter is investigated. The proposed control approach is designed to ensure: (i) efficient capture of wind aerodynamic energy; (ii) DC-link voltage regulation around its reference together with capacitor voltage balancing; and (iii) grid-side operation at unity power factor while reducing computational load. To achieve these objectives, a direct nonlinear control strategy based on FCS-MPC is employed. ISMC is adopted for the outer loops, and predictive current control with a new cost function minimization algorithm is used for the inner loops. The proposed algorithm reduces the number of evaluated switching states from 27 to 7 per sampling period. Moreover, a high-gain observer is designed to perform online estimation of the grid state variables that are not directly measurable, including grid voltages, angular frequency, and electrical angle, thereby reducing the need for additional grid sensors. A Lyapunov-based analysis is also provided to establish the uniform ultimate boundedness of the estimation error.

In this work, the sensorless approach estimates the PMSG mechanical speed and torque, as well as the grid voltages, angular frequency, and phase angle. Other variables, including wind speed, electrical currents, and DC-link capacitor voltages, are measured.

This paper presents the following contributions:

- A high-gain observer for sensorless estimation of grid voltages, angular frequency, and electrical angle.
- A hybrid ISMC–FCS-MPC framework for robust control of PMSG-based WECSs under parameter uncertainties and variable wind conditions.
- A two-stage FCS-MPC algorithm that reduces the evaluated switching states from 27 to 7 per sampling period.
- MATLAB/Simulink (R2024b) and Processor-in-the-Loop (PIL) evaluations using the LAUNCHXL-F28379D platform to assess control performance and computational efficiency.

The remaining content of this article is structured as follows: Section 2 presents the description and modeling of the wind energy conversion chain; Section 3 provides a detailed description of the observer design; Section 4 illustrates the development of the controller for the machine side and the grid side; Section 5 discusses the simulation results; and the final section concludes the paper.

2. System Modeling

The WECS consists of a turbine and a high-power PMSG connected to the grid via two 3L-NPC power converters, interfaced by a DC bus composed of two identical capacitors, as shown in Figure 1.

The turbine power coefficient is given by the following equation [21]:

$$C_{\mathrm{p}} = 0.576\left(\frac{116}{\lambda_{\mathrm{i}}} - 0.4\beta - 5\right)e^{\frac{-21}{\lambda_{\mathrm{i}}}} + 0.0068.\lambda \tag{1}$$

$$\lambda = \frac{\omega.R}{V_{\mathrm{v}}} \tag{2}$$

$$\frac{1}{\lambda_{\mathrm{i}}} = \frac{1}{\lambda+0.08\beta} - \frac{0.035}{\beta^3+1} \tag{3}$$

The tip-speed ratio and the blade pitch angle are represented by λ and β, respectively. The turbine blade radius is denoted by R, while the wind velocity and the angular speed are given by V_{v} and ω, respectively.

The aerodynamic power extracted from the wind turbine can be formulated as follows:

$$P_{\mathrm{a}} = \frac{1}{2}C_{\mathrm{p}}(\lambda,\beta).\rho.\pi.R^2.{V_{\mathrm{v}}}^3 \tag{4}$$

where ρ is the air density.

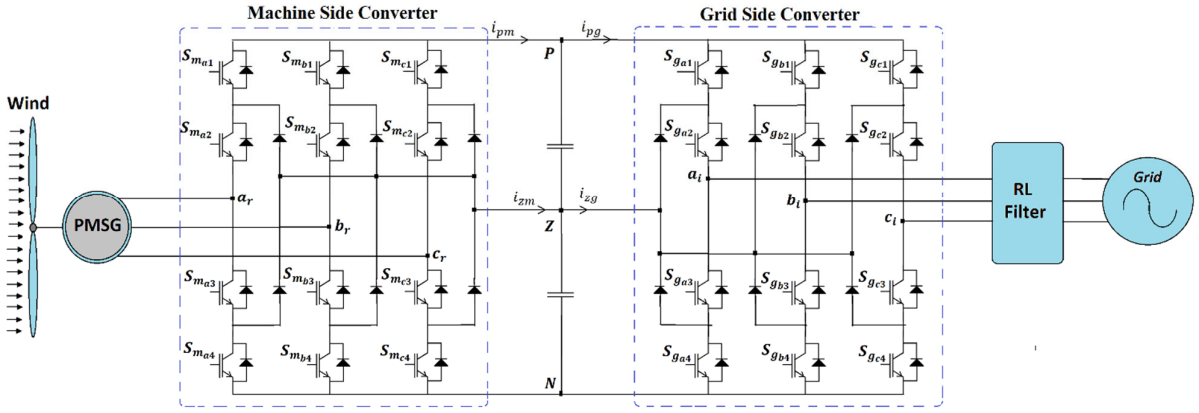


Figure 1. Overall structure of the WECS using a 3L-NPC converter. The arrows indicate the wind direction.

The PMSG continuous model is given by [22]:

$$\frac{di_{s\alpha}}{dt} = \frac{1}{L_s}\left(V_{s\alpha} - R_s i_{s\alpha} + p.\Omega\Phi_{r\beta}\right) \tag{5}$$

$$\frac{di_{s\beta}}{dt} = \frac{1}{L_s}\left(V_{s\beta} - R_s i_{s\beta} - p.\Omega\Phi_{r\alpha}\right) \tag{6}$$

$$\frac{d\Omega}{dt} = \frac{1}{J}(T_e - T_m - f_c\Omega) \tag{7}$$

where $V_{s\alpha}$, $V_{s\beta}$ and $i_{s\alpha}, i_{s\beta}$ denote the voltage and current of the machine in the $\alpha\beta$ reference frame; R_s is the stator resistance; L_s is the stator inductance of the PMSG; $(\Phi_{r\alpha}, \Phi_{r\beta})$ denote the rotor flux; and Ω is the rotor mechanical speed. T_e is the electromagnetic torque, p is the number of pole pairs of the PMSG, J is the total moment of inertia of the system, T_m is the mechanical torque, and f_c is the viscous friction.

The Euler method is applied over a sampling period T_s. Equations (5) and (6) then become [23]:

$$\begin{cases} i_{s\alpha}(k+1) = \left(1 - \frac{R_s T_s}{L_s}\right) i_{s\alpha}(k) + \frac{pT_s\Phi_{r\beta}}{L_s}.\Omega(k) + \frac{T_s}{L_s}V_{s\alpha}(k) \\ i_{s\beta}(k+1) = \left(1 - \frac{R_s T_s}{L_s}\right) i_{s\beta}(k) - \frac{pT_s\Phi_{r\alpha}}{L_s}.\Omega(k) + \frac{T_s}{L_s}V_{s\beta}(k) \end{cases} \tag{8}$$

The discrete representation of the GSC is given by:

$$\begin{cases} i_{g\alpha}(k+1) = \left(1 - \frac{R_f T_s}{L_f}\right) i_{g\alpha}(k) + \frac{T_s}{L_f}V_{i\alpha} - \frac{T_s}{L_f}V_{g\alpha} \\ i_{g\beta}(k+1) = \left(1 - \frac{R_f T_s}{L_f}\right) i_{g\beta}(k) + \frac{T_s}{L_f}V_{i\beta} - \frac{T_s}{L_f}V_{g\beta} \end{cases} \tag{9}$$

where $i_{g\alpha}, i_{g\beta}$ are the grid current, $(V_{i\alpha}, V_{i\beta})$ and $(V_{g\alpha}, V_{g\beta})$ are the inverter voltage and grid voltage in the $\alpha\beta$-frame, and L_f and R_f represent the filter inductance and resistance.

The DC-bus dynamics can be described as [24]:

$$\frac{1}{2}CV_{dc}\frac{dV_{dc}}{dt} = P_s - P_g \tag{10}$$

where $C = C_1 = C_2$, P_s is the power generated by the PMSG, and P_g is the active power delivered to the grid, given by [25]:

$$P_g = \frac{3}{2}\left(V_{gd}i_{gd} + V_{gq}i_{gq}\right) \tag{11}$$

For the two 3L-NPC converters, each leg is formed by four IGBTs and two clamping diodes. The control signals of the IGBTs are denoted as $S_{\Upsilon_{\chi j}}$ where $\chi \in \{a, b, c\}$ represents the phase name, $\Upsilon \in [m, g]$ indicates rectifier (m) or inverter (g), and $j \in \{1,2,3,4\}$ represents the switch number, as illustrated in Figure 1. The control of the upper and lower switches is complementary. For example, for phase (a) of the MSC, $S_{m_{a1}} = \overline{S}_{m_{a3}}$ and $S_{m_{a2}} = \overline{S}_{m_{a4}}$, and similarly for the other phases of the two converters. The DC bus includes two similar capacitors so that the net DC-bus voltage is equally distributed ($\frac{V_{dc}}{2} = V_{c1} = V_{c2}$). Three nodes are defined: the negative node (N), the positive node (P), and the neutral node (Z). The input terminals of the MSC and the output terminals of the GSC are alternated between (P), (N), and (Z). The number of possible combinations is 27 for each converter.

The prediction of the DC-bus capacitor voltages is given by the following relations [26]:

$$V_{c1}(k+1) = V_{c1}(k) + \frac{T_s}{C_1}\left(i_{pm}(k) - i_{pg}(k)\right) \tag{12}$$

$$V_{c2}(k+1) = V_{c2}(k) + \frac{T_s}{C_2}\left(i_{pm}(k) + i_{zm}(k) - i_{pg}(k) - i_{zg}(k)\right) \tag{13}$$

with $[V_{c1}(k), V_{c2}(k)]$ representing the voltages measured at time k across the capacitors, $[i_{\mathrm{pm}}(k), i_{\mathrm{zm}}(k))]$ are the currents entering the DC bus on the rectifier side, and $[i_{\mathrm{pg}}(k), i_{\mathrm{zg}}(k)]$ are the currents leaving the DC bus, which can be approximated by:

$$\begin{bmatrix} i_{\mathrm{pg}}(k) \\ i_{\mathrm{zg}}(k) \end{bmatrix} = \begin{bmatrix} S_{\mathrm{g_{a1}}}S_{\mathrm{g_{a2}}} & S_{\mathrm{g_{b1}}}S_{\mathrm{g_{b2}}} & S_{\mathrm{g_{c1}}}S_{\mathrm{g_{c2}}} \\ S_{\mathrm{g_{a2}}}S_{\mathrm{g_{a3}}} & S_{\mathrm{g_{b2}}}S_{\mathrm{g_{b3}}} & S_{\mathrm{g_{c2}}}S_{\mathrm{g_{c3}}} \end{bmatrix} \begin{bmatrix} i_{\mathrm{ga}} \\ i_{\mathrm{gb}} \\ i_{\mathrm{gc}} \end{bmatrix} \tag{14}$$

Depending on the applied combination, the inverter's terminals can be linked either to the potential (P), the potential (N), or the potential (Z) of the DC bus. The resulting voltages are given by the following relationship:

$$\begin{pmatrix} V_{\mathrm{a_iN}}(k) \\ V_{\mathrm{b_iN}}(k) \\ V_{\mathrm{c_iN}}(k) \end{pmatrix} = V_{\mathrm{c1}}(k) \begin{pmatrix} S_{\mathrm{g_{a1}}} \\ S_{\mathrm{g_{b1}}} \\ S_{\mathrm{g_{c1}}} \end{pmatrix} + V_{\mathrm{c2}}(k) \begin{pmatrix} S_{\mathrm{g_{a2}}} \\ S_{\mathrm{g_{b2}}} \\ S_{\mathrm{g_{c2}}} \end{pmatrix} \tag{15}$$

with $[V_{\mathrm{a_iN}}(k), V_{\mathrm{b_iN}}(k), V_{\mathrm{c_iN}}(k)]$ representing the voltages across the inverter outputs relative to the (N) potential.

The expression of the inverter output voltages in the $\alpha\beta$ reference frame is obtained by applying the Clarke transformation:

$$\begin{pmatrix} V_{\mathrm{i}\alpha}(k) \\ V_{\mathrm{i}\beta}(k) \end{pmatrix} = V_{\mathrm{c1}}(k) M_{\mathrm{abc/\alpha\beta}} \begin{pmatrix} S_{\mathrm{g_{a1}}} \\ S_{\mathrm{g_{b1}}} \\ S_{\mathrm{g_{c1}}} \end{pmatrix} + V_{\mathrm{c2}}(k) M_{\mathrm{abc/\alpha\beta}} \begin{pmatrix} S_{\mathrm{g_{a2}}} \\ S_{\mathrm{g_{b2}}} \\ S_{\mathrm{g_{c2}}} \end{pmatrix} \tag{16}$$

with $M_{\mathrm{abc/\alpha\beta}} = \frac{2}{3} \begin{pmatrix} 1 & -\frac{1}{2} & -\frac{1}{2} \\ 0 & \frac{\sqrt{3}}{2} & -\frac{\sqrt{3}}{2} \end{pmatrix}$ as the Clarke transformation matrix.

The equation above is used to predict the inverter output voltages at each sampling instant based on the switching states of the power devices.

Following the same analysis performed for the inverter, the input voltages on the machine-side converter are given by the following equation:

$$\begin{pmatrix} V_{\mathrm{a_rN}}(k) \\ V_{\mathrm{b_rN}}(k) \\ V_{\mathrm{c_rN}}(k) \end{pmatrix} = V_{\mathrm{c1}}(k) \begin{pmatrix} S_{\mathrm{m_{a1}}} \\ S_{\mathrm{m_{b1}}} \\ S_{\mathrm{m_{c1}}} \end{pmatrix} + V_{\mathrm{c2}}(k) \begin{pmatrix} S_{\mathrm{m_{a2}}} \\ S_{\mathrm{m_{b2}}} \\ S_{\mathrm{m_{c2}}} \end{pmatrix} \tag{17}$$

The input voltages of the rectifier in the $\alpha\beta$ frame are expressed by:

$$\begin{pmatrix} V_{\mathrm{s}\alpha}(k) \\ V_{\mathrm{s}\beta}(k) \end{pmatrix} = V_{\mathrm{c1}}(k) M_{\mathrm{abc/\alpha\beta}} \begin{pmatrix} S_{\mathrm{m_{a1}}} \\ S_{\mathrm{m_{b1}}} \\ S_{\mathrm{m_{c1}}} \end{pmatrix} + V_{\mathrm{c2}}(k) M_{\mathrm{abc/\alpha\beta}} \begin{pmatrix} S_{\mathrm{m_{a2}}} \\ S_{\mathrm{m_{b2}}} \\ S_{\mathrm{m_{c2}}} \end{pmatrix} \tag{18}$$

Equations (16) and (18) are used to establish the relationship between the AC-side voltages of the converters and the switching states of their switches.

For instance, for the switching combination $(S_{\mathrm{Y_{a1}}}S_{\mathrm{Y_{a2}}}S_{\mathrm{Y_{b1}}}S_{\mathrm{Y_{b2}}}S_{\mathrm{Y_{c1}}}S_{\mathrm{Y_{c2}}}) = (110000)$, the resulting voltage vector is:

$$\begin{pmatrix} V_{\alpha} \\ V_{\beta} \end{pmatrix} = V_{\mathrm{c1}} M_{\mathrm{abc/\alpha\beta}} \begin{pmatrix} 1 \\ 0 \\ 0 \end{pmatrix} + V_{\mathrm{c2}} M_{\mathrm{abc/\alpha\beta}} \begin{pmatrix} 1 \\ 0 \\ 0 \end{pmatrix} = \begin{pmatrix} \frac{4}{3} V_{\mathrm{c1}} \\ 0 \end{pmatrix} = V_7 \tag{19}$$

The same procedure is applied to the other 26 combinations. Table 1 presents all the combinations along with their corresponding voltage vectors, thereby summarizing the relationship between each switching combination and its voltage vector.

Table 1. Voltage vectors and corresponding switching combinations of the 3L-NPC converter.

Voltage vector	$\boldsymbol{V_0}$		$\boldsymbol{V_1}$	$\boldsymbol{V_2}$	$\boldsymbol{V_3}$	$\boldsymbol{V_4}$	$\boldsymbol{V_5}$
Switching combinations ($S_{Y_{a1}}S_{Y_{a2}}S_{Y_{b1}}S_{Y_{b2}}S_{Y_{c1}}S_{Y_{c2}}$)	(000000); (010101) (111111)		(010000) (110101)	(010100) (111101)	(011101) (000100)	(011111) (000101)	(010111) (000001)
Voltage vector	$\boldsymbol{V_6}$	$\boldsymbol{V_7}$	$\boldsymbol{V_8}$	$\boldsymbol{V_9}$	$\boldsymbol{V_{10}}$	$\boldsymbol{V_{11}}$	$\boldsymbol{V_{12}}$
Switching combinations ($S_{Y_{a1}}S_{Y_{a2}}S_{Y_{b1}}S_{Y_{b2}}S_{Y_{c1}}S_{Y_{c2}}$)	(110111) (010001)	(110000)	(110100)	(111100)	(011100)	(001100)	(001101)
Voltage vector	$\boldsymbol{V_{13}}$	$\boldsymbol{V_{14}}$	$\boldsymbol{V_{15}}$	$\boldsymbol{V_{16}}$	$\boldsymbol{V_{17}}$	$\boldsymbol{V_{18}}$	
Switching combinations ($S_{Y_{a1}}S_{Y_{a2}}S_{Y_{b1}}S_{Y_{b2}}S_{Y_{c1}}S_{Y_{c2}}$)	(001111)	(000111)	(000011)	(010011)	(110011)	(110001)	

The distribution of the 19 voltage vectors in the αβ plane is shown in Figure 2.

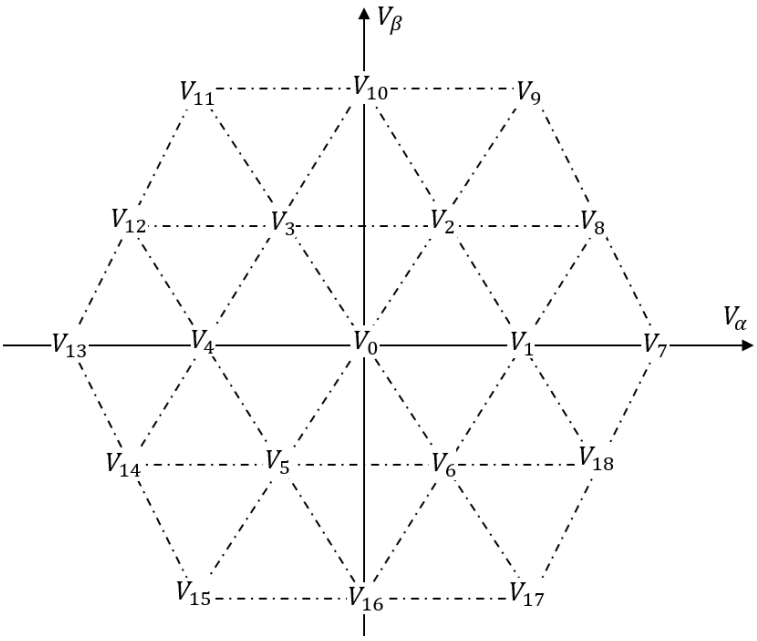


Figure 2. Space vector diagram of the 3L-NPC converter.

3. Grid Observer

The objective of this section is to develop a grid-side observer capable of estimating the electrical grid variables that are not directly measured, namely the grid voltages $V_{g\alpha}, V_{g\beta}$, as well as the grid angular frequency w_g and electrical angle θ_g. This estimation enhances the reliability of the WECS by reducing the need for additional sensors. Consider the following grid-side model [27]:

$$\begin{cases} \frac{di_{g\alpha}}{dt} = -\frac{R_f}{L_f} i_{g\alpha} + \frac{V_{i\alpha}}{L_f} - \frac{V_{g\alpha}}{L_f} \\ \frac{di_{g\beta}}{dt} = -\frac{R_f}{L_f} i_{g\beta} + \frac{V_{i\beta}}{L_f} - \frac{V_{g\beta}}{L_f} \\ \frac{dV_{g\alpha}}{dt} = w_g \sqrt{{V_{g\alpha}}^2 + {V_{g\beta}}^2} \cos(\theta_g) \\ \frac{dV_{g\beta}}{dt} = w_g \sqrt{{V_{g\alpha}}^2 + {V_{g\beta}}^2} \sin(\theta_g) \\ \frac{d\theta_g}{dt} = w_g \\ \frac{dw_g}{dt} = \beta_1(t) \end{cases} \quad (20)$$

where w_g and θ_g denote the grid angular frequency and the grid phase angle, respectively. The term $\beta_1(t)$ represents a bounded, unknown, time-varying function.

The relationship between the amplitude of the grid electromotive force E_g and the voltage components $V_{g\alpha}$ and $V_{g\beta}$ is given as follows: $E_g = \sqrt{{V_{g\alpha}}^2 + {V_{g\beta}}^2}$

Model (20) can be rewritten in the following form:

$$\begin{cases} \dot{X}(t) = g\big(X(t), u(t)\big) + \beta(t) \\ Y(t) = C.X(t) \end{cases} \tag{21}$$

With $X = \begin{bmatrix} X_1 \\ X_2 \\ X_3 \end{bmatrix}$, where $X_1 = [x_{11}\ x_{12}]^T = \left[i_{g\alpha}\ i_{g\beta}\right]^T$ represents the measured variables, $X_2 = [x_{21}\ x_{22}]^T = \left[V_{g\alpha}\ V_{g\beta}\right]^T$ and $X_3 = [x_{31}\ x_{32}]^T = \left[\theta_g\ w_g\right]^T$ and $\beta(t) = [0\ 0\ 0\ 0\ 0\ \beta_1(t)\ ]^T$ $C = [\mathrm{I}_2\ \mathrm{O}_2\ \mathrm{O}_2]$, where I_2 and O_2 denote, respectively, the identity matrix and the zero matrix of order 2.

The dynamic vector is given by:

$$g\big(X(t), u(t)\big) = \begin{pmatrix} -\frac{R_f}{L_f}x_{11} + \frac{V_{i\alpha}}{L_f} - \frac{x_{21}}{L_f} \\ -\frac{R_f}{L_f}x_{12} + \frac{V_{i\beta}}{L_f} - \frac{x_{22}}{L_f} \\ x_{32}\sqrt{{x_{21}}^2 + {x_{22}}^2}\cos(x_{31}) \\ x_{32}\sqrt{{x_{21}}^2 + {x_{22}}^2}\sin(x_{31}) \\ x_{32} \\ 0 \end{pmatrix} \tag{22}$$

Assume that a Lipschitz diffeomorphism $\Phi(X)$ exists. The transformation of System (21) from X to Z can be written as follows:

$$\Phi(X): X \to Z = \begin{pmatrix} Z_1 \\ Z_2 \\ Z_3 \end{pmatrix};\ \Phi(X) = \begin{pmatrix} \Phi_1(X) \\ \Phi_2(X) \\ \Phi_3(X) \end{pmatrix} \tag{23}$$

where

$$\begin{cases} Z_1 = \begin{bmatrix} z_{11} \\ z_{12} \end{bmatrix} = \begin{bmatrix} x_{11} \\ x_{12} \end{bmatrix} \\ Z_2 = \begin{bmatrix} z_{21} \\ z_{22} \end{bmatrix} = \begin{bmatrix} -\frac{x_{21}}{L_f} \\ -\frac{x_{22}}{L_f} \end{bmatrix} \\ Z_3 = \begin{bmatrix} z_{31} \\ z_{32} \end{bmatrix} = \begin{bmatrix} -\frac{x_{32}}{L_f}\sqrt{{x_{21}}^2 + {x_{22}}^2}\cos(x_{31}) \\ -\frac{x_{32}}{L_f}\sqrt{{x_{21}}^2 + {x_{22}}^2}\sin(x_{31}) \end{bmatrix} \end{cases} \tag{24}$$

The system dynamics in the Z coordinates are expressed as follows:

$$\begin{cases} \dot{z}_1 = z_2 + f_1(z_1, u) \\ \dot{z}_2 = z_3 + f_2 \\ \dot{z}_3 = f_3(z, u) + \chi(\mathrm{z})\beta(\mathrm{t}) \end{cases} \tag{25}$$

with

$$\begin{cases} f_1 = \begin{pmatrix} -\frac{R_f}{L_f} z_{11} + \frac{V_{i\alpha}}{L_f} \\ -\frac{R_f}{L_f} z_{12} + \frac{V_{i\beta}}{L_f} \end{pmatrix} \\ f_2 = \begin{pmatrix} 0 \\ 0 \end{pmatrix} \\ f_3 = \begin{pmatrix} -x_{32} z_{32} \\ x_{32} z_{31} \end{pmatrix} \\ \chi(z)\beta(t) = \begin{pmatrix} -\frac{1}{L_f} \sqrt{{x_{21}}^2 + {x_{22}}^2} \cos(x_{31}) \beta_1(t) \\ -\frac{1}{L_f} \sqrt{{x_{21}}^2 + {x_{22}}^2} \sin(x_{31}) \beta_1(t) \end{pmatrix} \end{cases} \quad (26)$$

System (25) can be written in the following form:

$$\begin{cases} \dot{z}(t) = Az(t) + f(z,u) + B\chi(z)\beta(t) \\ y(t) = C.z(t) \end{cases} \quad (27)$$

where $f(z,u) = \begin{pmatrix} f_1 \\ f_2 \\ f_3 \end{pmatrix}$; $A = \begin{pmatrix} 0_2 & I_2 & 0_2 \\ 0_2 & 0_2 & I_2 \\ 0_2 & 0_2 & 0_2 \end{pmatrix}$; and $B = \begin{pmatrix} 0_2 \\ 0_2 \\ I_2 \end{pmatrix}$

Assumptions 1.

- *The unknown time-varying function* $\beta(t)$ *is uniformly bounded, i.e.,*

$$\exists \beta_0 > 0;\ \forall\, t \geq 0: \|\beta(t)\| \leq \beta_0 \quad (28)$$

- *The grid voltage amplitude is constant and strictly positive, and the grid angular frequency is bounded:*

$$E_g = E_0 > 0;\ \ 0 < w_{min} \leq w_g \leq w_{max} \quad (29)$$

The actual and estimated trajectories are assumed to remain within a bounded admissible operating domain consistent with the grid voltage model. The grid phase angle is considered modulo 2π.

Checking the observability of System (27) is an essential step. For this purpose, we compute the Jacobian of the diffeomorphism corresponding to the considered transformation.

$$\Lambda = \frac{\partial \Phi(X)}{\partial X} = \begin{pmatrix} 1 & 0 & 0 & 0 & 0 & 0 \\ 0 & 1 & 0 & 0 & 0 & 0 \\ 0 & 0 & -\frac{1}{L_f} & 0 & 0 & 0 \\ 0 & 0 & 0 & -\frac{1}{L_f} & 0 & 0 \\ 0 & 0 & -\frac{x_{32}x_{21}}{L_f E_g}\cos(x_{31}) & -\frac{x_{32}x_{22}}{L_f E_g}\cos(x_{31}) & \frac{x_{32}E_g}{L_f}\sin(x_{31}) & \frac{-E_g}{L_f}\cos(x_{31}) \\ 0 & 0 & -\frac{x_{32}x_{21}}{L_f E_g}\sin(x_{31}) & -\frac{x_{32}x_{22}}{L_f E_g}\sin(x_{31}) & -\frac{x_{32}E_g}{L_f}\cos(x_{31}) & \frac{-E_g}{L_f}\sin(x_{31}) \end{pmatrix} \quad (30)$$

In order to determine the rank of the Jacobian, we compute its determinant.

$$\det(\Lambda) = -\frac{1}{{L_f}^4} x_{32}({x_{21}}^2 + {x_{22}}^2) = -\frac{1}{{L_f}^4} w_g {E_g}^2 \quad (31)$$

The determinant of the Jacobian matrix is nonzero when $w_g \neq 0$ and $E_g \neq 0$. Therefore, the Jacobian is full rank, and the transformation $\Phi(X)$ is locally invertible, allowing the system states to be locally reconstructed.

Based on the transformed model, the high-gain observer is defined as follows [25]:

$$\dot{\hat{Z}}(t) = A\hat{Z}(t) + f(\hat{Z},u) - \theta {\Delta_\theta}^{-1} KC(\hat{Z}(t) - Z(t)) \quad (32)$$

where θ is a positive observer parameter, Δ_θ is a diagonal matrix given by:

$$\Delta_\theta = diag(\mathrm{I}_2, \frac{1}{\theta}\mathrm{I}_2, \frac{1}{\theta^2}\mathrm{I}_2)$$

and $K \epsilon \mathbb{R}^{6\times 2}$ is the observer gain matrix.

Based on the Routh–Hurwitz criterion, the matrix $(A - KC)$ is Hurwitz if the gain K is chosen as follows:

$$K = \begin{pmatrix} 3b\mathrm{I}_2 \\ 3b^2\mathrm{I}_2 \\ b^3\mathrm{I}_2 \end{pmatrix} \tag{33}$$

where b is a positive parameter.

Proposition 1. *Consider the transformed system and the proposed observer. Under the stated assumptions, and provided that the matrix* $(A - KC)$ *is Hurwitz, there exists a constant* $\theta_0 > 1$ *such that, for any observer gain* $\theta > \theta_0$*, the estimation error* $\tilde{z}(\mathrm{t}) = \hat{z}(t) - z(t))$ *is uniformly ultimately bounded. Moreover, its ultimate bound can be made arbitrarily small by sufficiently increasing* θ.

Proof. Define the scaled estimation error as

$$e_z(t) = \Delta_\theta \tilde{z}(t)$$

The scaled error dynamics are given by

$$\dot{e}_z = \theta(A - KC)e_z + \Delta_\theta[f(\hat{z}, u) - f(z, u) - \mathrm{B}\chi(\mathrm{z})\beta(\mathrm{t})] \tag{34}$$

The matrix $A - KC$ is Hurwitz. Let us choose a symmetric positive-definite matrix P such that:

$$(A - KC)^T P + P(A - KC) \leq -2\tau \mathrm{I}_6; \tag{35}$$

where $\tau > 0$.

Consider the Lyapunov function:

$$V = \frac{1}{2} e_z^T P e_z \tag{36}$$

Differentiating V along the error trajectories yields

$$\dot{V} \leq -\tau\theta \|e_z\|^2 + e_z^T P \Delta_\theta [f(\hat{z}, u) - f(z, u) - \mathrm{B}\chi(\mathrm{z})\beta(\mathrm{t})] \tag{37}$$

From the structure of the nonlinear function $f(z, u)$ and the boundedness of the grid angular frequency, the following scaled Lipschitz inequality holds on the considered admissible domain:

$$\|\Delta_\theta [f(\hat{z}, u) - f(z, u)]\| \leq K_n \|e_z\| \tag{38}$$

where $K_n = \max\left\{\frac{R_f}{L_f}, 2w_{max}\right\}$

Moreover, since

$$\begin{cases} \Delta_\theta B = \frac{1}{\theta^2} B \\ \|\chi(\mathrm{z})\| = \frac{E_g}{L_f} \end{cases} \tag{39}$$

the disturbance term satisfies

$$\|\Delta_\theta B \chi(\mathrm{z})\beta(\mathrm{t})\| \leq \frac{E_g \beta_0}{L_f \theta^2} \tag{40}$$

Let γ_{max} and γ_{min} be the maximum and minimum eigenvalues of P, respectively. Using Equations (38) and (40), we obtain

$$\dot{V} \leq (\gamma_{max} K_n - \tau\theta)\|e_z\|^2 + \frac{\gamma_{max} E_g \beta_0}{L_f \theta^2}\|e_z\| \tag{41}$$

For $\theta > \max\left\{1, \frac{\gamma_{max} K_n}{\tau}\right\}$

Define $a_\theta = \tau\theta - \gamma_{max} K_n > 0$

Using the eigenvalue inequalities

$$\frac{1}{2}\gamma_{min}\|e_z\|^2 \leq V \leq \frac{1}{2}\gamma_{max}\|e_z\|^2 \tag{42}$$

we obtain

$$\dot{V} \leq -\frac{2a_\theta}{\gamma_{max}} V + \frac{\gamma_{max} E_g \beta_0}{L_f \theta^2}\sqrt{\frac{2}{\gamma_{min}} V} \tag{43}$$

Let $F = \sqrt{V}$

$$\dot{F} \leq -\frac{a_\theta}{\gamma_{max}} F + \frac{\gamma_{max} E_g \beta_0}{L_f \theta^2 \sqrt{2\gamma_{min}}} \tag{44}$$

By applying the standard comparison lemma, we obtain

$$F(t) \leq F(0) e^{-\frac{a_\theta}{\gamma_{max}} t} + \frac{{\gamma_{max}}^2 E_g \beta_0}{L_f \theta^2 a_\theta \sqrt{2\gamma_{min}}}\left(1 - e^{-\frac{a_\theta}{\gamma_{max}} t}\right) \tag{45}$$

Since $a_\theta > 0$,

$$\lim_{t\to\infty} Sup\, F(t) \leq \frac{{\gamma_{max}}^2 E_g \beta_0}{L_f \theta^2 a_\theta \sqrt{2\gamma_{min}}} \tag{46}$$

Furthermore, using the eigenvalue inequality, we have

$$\|e_z\| \leq \sqrt{\frac{2}{\gamma_{min}}} F \tag{47}$$

Consequently, the ultimate bound of the scaled estimation error is given by

$$\lim_{t\to\infty} Sup\, \|e_z(t)\| \leq \frac{{\gamma_{max}}^2 E_g \beta_0}{L_f \theta^2 a_\theta \gamma_{min}} \tag{48}$$

Since

$$\tilde{z} = {\Delta_\theta}^{-1} e_z;\ \left\|{\Delta_\theta}^{-1}\right\| = \theta^2 \tag{49}$$

it follows that

$$\lim_{t\to\infty} Sup\, \|\tilde{z}(t)\| \leq \frac{{\gamma_{max}}^2 E_g \beta_0}{L_f (\tau\theta - \gamma_{max} K_n) \gamma_{min}} \tag{50}$$

Thus, under the stated assumptions, the estimation error in the transformed coordinates is uniformly ultimately bounded, and its ultimate bound can be made arbitrarily small by sufficiently increasing the observer gain.

This concludes the proof of the proposition. □

For implementation, the observer is expressed in the original coordinates x. By applying the inverse of the Jacobian matrix associated with the diffeomorphism, the observer structure is obtained as follows:

$$\dot{\hat{X}}(t) = g\left(\hat{X}, u\right) - \theta \Lambda^{-1} {\Delta_\theta}^{-1} K C(\hat{X}(t) - X(t)) \tag{51}$$

4. Control Design

The control scheme of the WECS, consists of two controllers, one for the MSC and the other for the GSC, in order to achieve the following objectives:

- Maximum power point tracking: The rotational speed must converge to the reference provided by the MPPT block to improve power extraction efficiency.

- Regulation of the DC-bus voltage and maintaining balance between the voltages of the two capacitors in the DC link.
- Management of the power transferred between the DC bus and the grid, ensuring a unity power factor on the grid side.
- Optimization of the cost function minimization algorithm to reduce the computational load.

4.1. Machine-Side Converter Control

The generator-side controller is composed of two control loops: an outer loop for the machine's rotational speed, which provides the quadrature current reference for the inner current control loop, and an inner loop for current regulation.

Remark 1. *An observer for estimating the mechanical torque and rotor speed of the PMSG from the measured stator currents was developed and validated in [25]. In this work, the same observer is used to obtain the rotor speed* $\widehat{\Omega}$ *and mechanical torque of the PMSG, which are then used in the MSC control.*

4.1.1. Outer Loop

The reference speed of the PMSG corresponding to the maximum power point (MPPT) is generated using an artificial neural network (ANN). This reference depends on two variables: wind speed and blade pitch angle. The ANN provides a direct estimation of the optimal reference speed, avoiding online optimization of the aerodynamic power coefficient. Although an analytical relation or a lookup table could also be used, the ANN offers an alternative approach to approximating the nonlinear relationship between these variables.

The operation of a neural network is inspired by the functioning of the human brain. It consists of numerous neurons interconnected through synapses associated with numerical weights and organized into different layers. The mathematical representation of a neuron can be expressed as follows [28]:

$$S = f\left(\sum_{\mathrm{i}}^{\mathrm{n}} w_{\mathrm{i}} x_{\mathrm{i}} + b\right) \tag{52}$$

where S is the output of the neuron, f is the activation function, x_i are the inputs to the neuron, b is the bias, and w_{i} are the weights of the input synapses.

The first phase of designing and developing the neural network involves collecting the training data necessary for its learning. In our case, this data collection relies on the analysis of the turbine's power coefficient, defined by Equation (1). For each value of wind velocity and blade pitch angle, the rotational speed that maximizes the power coefficient is determined. This approach provides a representative dataset of the turbine's optimal operating conditions. A database consisting of 14,326 samples was created, with each sample containing three values: wind speed, pitch angle, and optimal mechanical speed.

The dataset covers wind speeds ranging from 2 to 13 m/s and blade pitch angles from 0 to 25°. The input data were normalized using the MATLAB mapminmax function, and the inverse transformation was automatically applied at the network output to recover the optimal mechanical speed in its original scale.

The dataset is then split into three subsets following the proportions below:

- Training, 70%;
- Testing, 15%;
- Validation, 15%.

The choice of the neural network structure is not deterministic, meaning there is no rule to define an optimal structure. In our case, a trial-and-error approach was used to

identify the optimal neural network structure, based on the analysis of the regression coefficient and the mean squared error, defined by [29,30]:

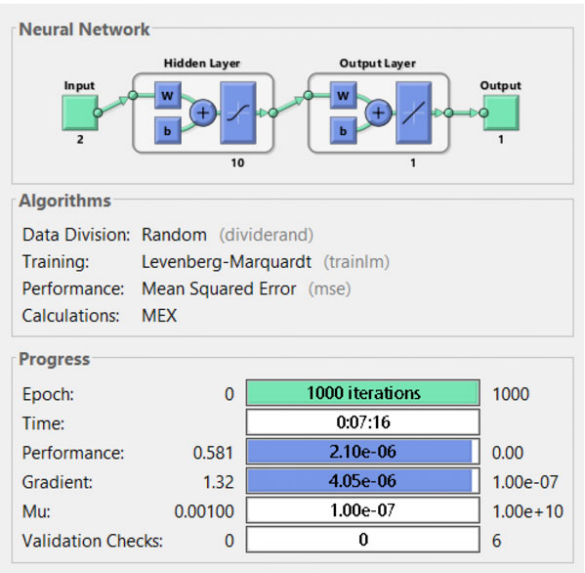
$$R = \frac{\sum_{i=1}^{n}\left(S_i^{ANN} - \overline{S^{ANN}}\right)\left(S_i^{Tar} - \overline{S^{Tar}}\right)}{\sqrt{\left[\sum_{i=1}^{n}\left(S_i^{ANN} - \overline{S^{ANN}}\right)^2\right]\left[\sum_{i=1}^{n}\left(S_i^{Tar} - \overline{S^{Tar}}\right)^2\right]}} \quad (53)$$

$$MSE = \frac{1}{n}\sum_{i=1}^{n}\left(S_i^{ANN} - S_i^{Tar}\right)^2 \quad (54)$$

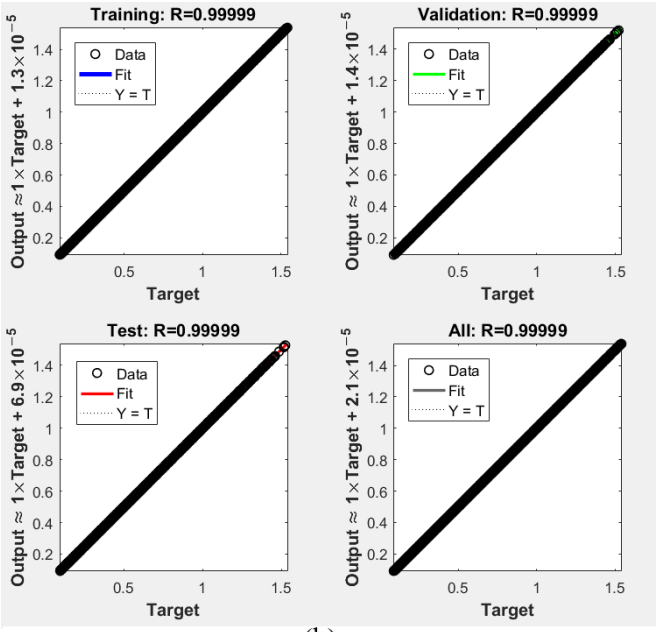
where S_i^{ANN} and S_i^{Tar} represent the predicted output of the ANN and the corresponding target value for the $i-th$ sample, respectively. $\overline{S^{ANN}}$ and $\overline{S^{Tar}}$ denote the mean values of the predicted and target outputs, respectively, and n is the total number of samples.

The developed neural network has two inputs: wind velocity and pitch angle. It includes a single hidden layer composed of 10 neurons, followed by an output layer that generates the reference speed. The hyperbolic tangent (tansig) activation function is applied in the hidden layer, whereas a linear activation function is used at the output. The training process is carried out using the Levenberg–Marquardt algorithm, which updates the weights and biases to optimize the model's accuracy. Figure 3 shows the structure of the proposed ANN as well as its training performance. The model achieves a mean squared error of 2.1×10^{-6} and a regression coefficient of R = 0.9999, indicating high accuracy.

The ANN-MPPT is trained using data generated from the theoretical wind turbine model. Therefore, its accuracy depends on the turbine model parameters used during training. Variations in the actual aerodynamic characteristics may affect the estimation of the optimal reference speed and, consequently, the MPPT performance.



(a)



(b)

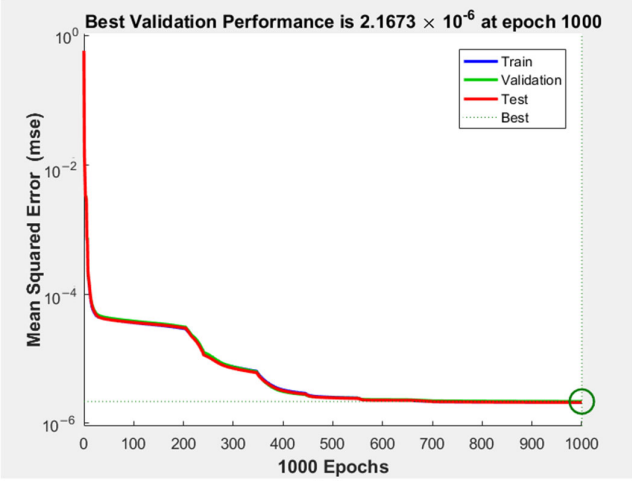


Figure 3. MPPT with artificial neural network: (**a**) Structure, (**b**) regression coefficient (R), (**c**) performance (MSE). In (**b**), the black circles represent the regression data points.

For the speed control loop, a nonlinear control strategy based on ISMC was adopted. The integral action was incorporated due to its ability to attenuate disturbances, reduce tracking error as well as steady-state error and limit the chattering effect.

The sliding surface is given by [25]:

$$S(x) = \left(\frac{\partial}{\partial t} + \delta\right)^{n-1} e(x) + K_{\mathrm{i}} \int e(x) \tag{55}$$

where $e(x)$ *and* n denote the error and the relative degree, respectively, while the parameters K_{i} and δ are positive values.

Let us consider the following sliding surface:

$$S_{\Omega} = e_{\Omega} + K_1 \int e_{\Omega} \tag{56}$$

where $e_{\mathrm{w}} = \widehat{\Omega} - \Omega_{\mathrm{ref}}$ and $K_1 > 0$.

The temporal derivative of S_{Ω} is expressed by:

$$\dot{S}_{\Omega} = \frac{1}{J}\left[\mathrm{T_e} - \hat{T}_{\mathrm{m}} - f_{\mathrm{c}}\widehat{\Omega}\right] - \dot{\Omega}_{\mathrm{ref}} + K_1 e_{\Omega} \tag{57}$$

$$\dot{S}_{\Omega} = \frac{1}{J}\left[\frac{3}{2} p \Phi_{\mathrm{f}} \mathrm{i_{sq}} - \hat{T}_{\mathrm{m}} - f_{\mathrm{c}}\widehat{\Omega}\right] - \dot{\Omega}_{\mathrm{ref}} + K_1 e_{\Omega} \tag{58}$$

The equivalent control law is obtained from the condition:

$$\dot{S}_{\Omega} = 0 \tag{59}$$

$$i_{\mathrm{sq-eq}} = \frac{2}{3p\Phi_{\mathrm{f}}}\left[\hat{T}_{\mathrm{m}} + f_{\mathrm{c}}\widehat{\Omega} + J\,\dot{\Omega}_{\mathrm{ref}} - K_1 J e_{\Omega}\right] \tag{60}$$

To analyze stability, we define a Lyapunov function as:

$$V_1 = \frac{1}{2} {S_{\Omega}}^2 \tag{61}$$

Its time derivative is then computed as follows:

$$\dot{V}_1 = \frac{3p\Phi_{\mathrm{f}}}{2\mathrm{J}} S_{\Omega} . i_{\mathrm{sq-dis}} \tag{62}$$

The following discontinuous control law has been chosen:

$$i_{\mathrm{sq-dis}} = -\frac{2JK_2}{3p\Phi_{\mathrm{f}}} . \frac{S_{\Omega}}{|S_{\Omega}| + \varepsilon_1} \tag{63}$$

where K_2 is a positive parameter, and ε_1 is a small positive parameter.

By applying Equations (62) and (63), the Lyapunov function's derivative will be of the following form:

$$\dot{V}_1 = -K_2 \frac{S_\Omega^2}{|S_\Omega|+\varepsilon_1} < 0 \tag{64}$$

Thus, the sliding surface converges to zero, provided that current tracking and state estimation are ideal.

The control law is expressed by:

$$i_{\mathrm{sq-ref}} = \frac{2}{3p\Phi_\mathrm{f}}\left[\hat{T}_\mathrm{m} + f_\mathrm{c}\hat{\Omega} + J\,\dot{\Omega}_\mathrm{ref} - K_1 J e_\Omega - K_2 J \frac{S_\Omega}{|S_\Omega|+\varepsilon_1}\right] \tag{65}$$

4.1.2. Inner Loop

The inner loops on the machine side regulate the PMSG stator currents, maintain stable electromagnetic torque, and maximize the extracted power. The next sections describe tow predictive control methods.

a. Conventional FCS-MPC

In this predictive control approach, the selection of the optimal combination of the rectifier's switching states is based on minimizing the following cost function:

$$f_{\mathrm{c_m}} = [i_{\mathrm{s}\alpha}(k+1) - i^*_{\mathrm{s}\alpha}(k+1)]^2 + \left[i_{\mathrm{s}\beta}(k+1) - i^*_{\mathrm{s}\beta}(k+1)\right]^2 + \lambda_{\mathrm{c_s}} \sum_{\chi=\mathrm{a,b,c}} \sum_{\mathrm{j}=1,2} \left[S_{\mathrm{m}_{\chi\mathrm{j}}} - S^{\mathrm{op}}_{\mathrm{m}_{\chi\mathrm{j}}}\right]^2 \tag{66}$$

where $\lambda_{\mathrm{c-s}}$ represents a weighting coefficient, and $S^{\mathrm{op}}_{\mathrm{m}_{\chi\mathrm{j}}}$ is the optimal control signal found at the previous time step. This function evaluates the deviation between the predicted stator currents and their references while optimizing the switching frequency through the weighting coefficient $\lambda_{\mathrm{c-s}}$. This coefficient defines the importance given to the reduction of the switching frequency.

A low value of $\lambda_{\mathrm{c-s}}$ improves the accuracy of stator current tracking, providing a faster dynamic response and limiting torque ripple. This helps maintain smooth operation of the WECS. However, this value leads to higher switching frequency of the rectifier switches, which raises switching losses and reduces the lifespan of the power electronics switches. Conversely, a high value of $\lambda_{\mathrm{c-s}}$ minimizes the switching frequency at the cost of reduced accuracy and slower dynamics of the current control loops. The selection of this coefficient is crucial to achieving an optimal trade-off between reducing switching losses and meeting control objectives.

The prediction of the currents $i_{\mathrm{s}\alpha}(k+1)$ and $i_{\mathrm{s}\beta}(k+1)$ is performed using Model (8). In this model, the mechanical speed and the currents $i_{s\alpha}(k)$ and $i_{\mathrm{s}\beta}(k)$ are directly measurable, while the voltages $\left(V_{\mathrm{s}\alpha}(k), V_{\mathrm{s}\beta}(k)\right)$ are predicted using Expression (18). The cost function also incorporates the reference currents $i^*_{\mathrm{s}\alpha}(k+1)$ and $i^*_{\mathrm{s}\beta}(k+1)$, which are extrapolated from instant k using the fourth-order Lagrange extrapolation method according to the following relation:

$$i^*_{\mathrm{s}\alpha\beta}(k+1) = 4i^*_{\mathrm{s}\alpha\beta}(k) - 6i^*_{\mathrm{s}\alpha\beta}(k-1) + 4i^*_{\mathrm{s}\alpha\beta}(k-2) - i^*_{\mathrm{s}\alpha\beta}(k-3) \tag{67}$$

Conventional MPC relies on the exhaustive exploration of the 27 possible configurations of the three-level rectifier to identify the optimal combination. At each iteration, the system variables are predicted for each configuration, and the cost function is then calculated to assess the performance of each candidate solution. The combination that yields the minimum value is applied to the rectifier in the following control step. Figure 4a shows a clear illustration of the different steps of the conventional FCS-MPC.

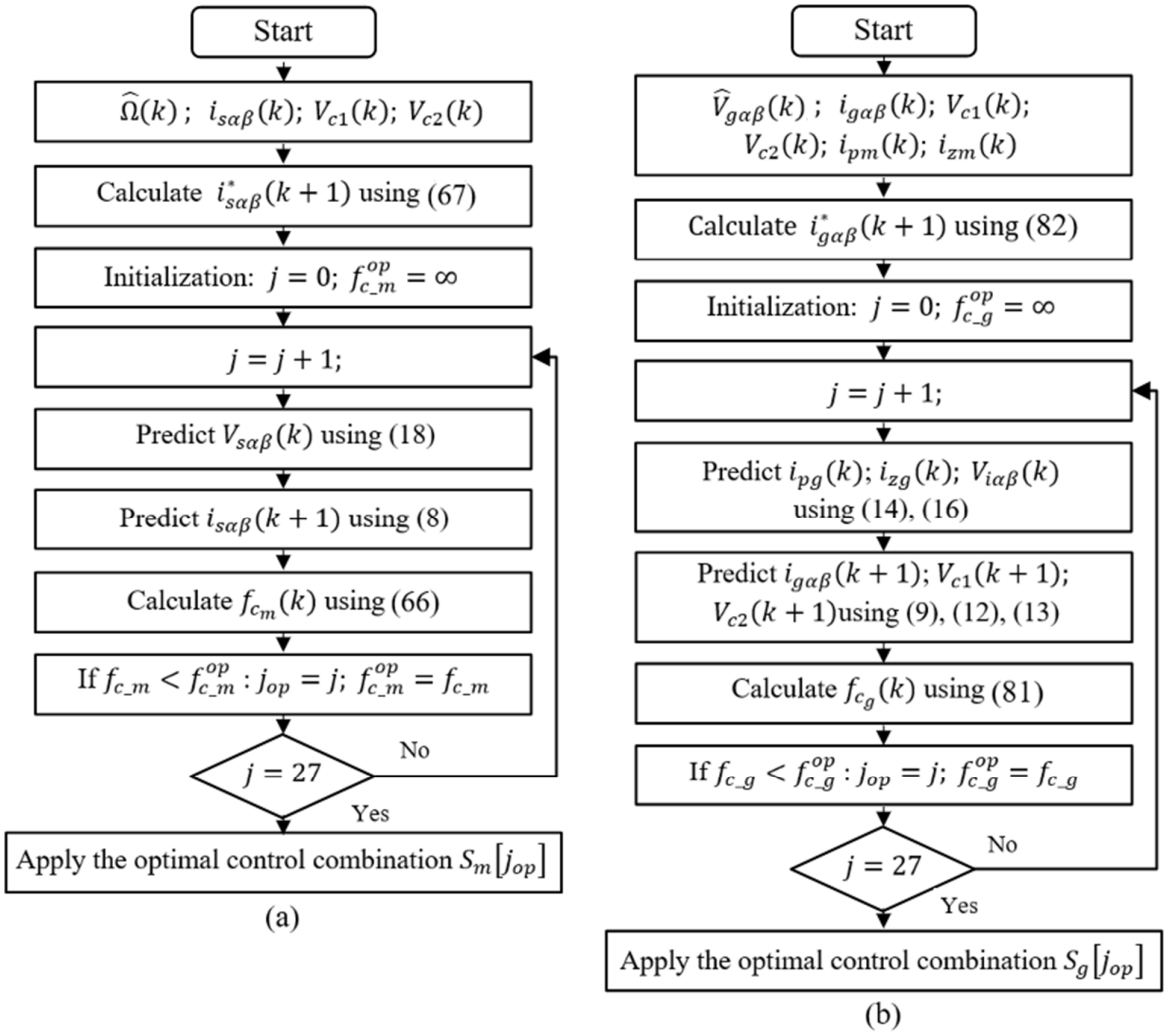


Figure 4. Flowchart of the conventional FCS-MPC: (**a**) MSC; (**b**) GSC.

b. Proposed FCS-MPC

The main challenge of predictive control lies in its high computational burden. Indeed, in conventional FCS-MPC, at each sampling period, the algorithm must evaluate all 27 switching combinations in order to determine the optimal control action. This exhaustive search over the complete voltage vector diagram leads to a significant computational cost.

The idea of the proposed method is to reduce the number of evaluations performed in each computation cycle. To reduce the computational burden, the proposed strategy restricts the search to a reduced subset of admissible switching states instead of evaluating all 27 possible combinations. This reduction is motivated by the observation that the optimal switching state is generally associated with a voltage vector located close to the reference voltage vector in the $\alpha\beta$ plane. Consequently, the reduced search space preserves a near-optimal control action while significantly decreasing the computational effort.

To achieve this objective, the proposed control strategy is composed of two main stages: the identification of the sector containing the optimal solution, followed by the selection of the optimal switching combination within that sector.

- **Step 1**: Sector identification

The objective of this phase is to identify the region containing the optimal switching combination in order to reduce the computational burden of the predictive control algorithm.

Instead of evaluating all 27 possible switching combinations of the 3L-NPC converter, the search space is restricted to a reduced subset associated with a specific region of the $\alpha\beta$ plane.

From the discrete Model (8), the reference voltage vector in the $\alpha\beta$ reference frame is calculated as follows in order to ensure stator current tracking:

$$\begin{cases} V_{s\alpha}^{ref}(k) = \frac{L_s}{T_s} i_{s\alpha}^{*}(k+1) + \left(R_s - \frac{L_s}{T_s}\right) i_{s\alpha}(k) - p\Phi_{r\beta}\widehat{\Omega}(k) \\ V_{s\beta}^{ref}(k) = \frac{L_s}{T_s}.\, i_{s\beta}^{*}(k+1) + \left(R_s - \frac{L_s}{T_s}\right) i_{s\beta}(k) + p\Phi_{r\alpha}\widehat{\Omega}(k) \end{cases} \quad (68)$$

where the reference currents $i_{s\alpha}^{*}(k+1)$ and $i_{s\beta}^{*}(k+1)$ are extrapolated from instant k using the fourth-order Lagrange extrapolation method.

This reference voltage vector is not directly applied to the converter; it is used as an intermediate indicator, derived from the system dynamics, in order to locate the desired operating point in the $\alpha\beta$ plane. The $\alpha\beta$ plane is split into four sectors according to the sign of $V_{s\alpha}^{ref}$ and $V_{s\beta}^{ref}$, as illustrated in Figure 5. This classification allows for the rapid identification of the optimal sector, following the method described in Table 2.

Table 2. Sector identification.

Sector	$V_{s\alpha}^{ref}$	$V_{s\beta}^{ref}$
Sector 1	Positive	Positive
Sector 2	Negative	Positive
Sector 3	Negative	Negative
Sector 4	Positive	Negative

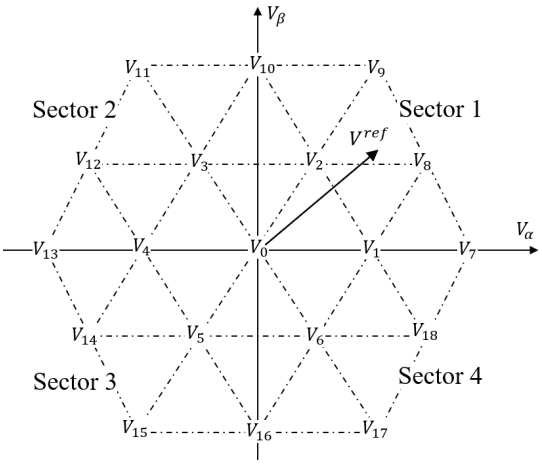


Figure 5. Space vector diagram of the 3L-NPC converter and its sectors.

By analyzing the sign of the components of the calculated reference voltage, it is possible to determine the sector containing the optimal control combination to be applied at the next instant. For instance, if Sector 1 is identified, the search space is restricted to the switching states associated with the nearest voltage vectors in this region, namely $(V_0, V_1, V_2, V_7, V_8, V_9, V_{10})$.

This can be explained by the observation that, in predictive control, the optimal voltage vector is typically located close to the reference voltage vector. Consequently, distant vectors are not considered, as they lead to larger tracking errors and do not allow the cost function to be minimized. This sector identification reduces the search space of the optimization problem, decreasing the number of possible combinations from 27 to 11. As a result, 16 prediction iterations are eliminated compared to the conventional MPC, thereby improving computational efficiency.

- **Step 2: Selection of the optimal combination for the MSC**

After identifying the sector, this stage consists of selecting the optimal combination within the sector determined in the previous phase. Before evaluating the candidate combinations associated with this sector, an analysis of the influence of the different voltage vectors on the DC-link balancing is carried out in order to reduce the number of combinations to be tested.

The voltage vectors $(V_0, V_7, V_9, V_{11}, V_{13}, V_{15}, V_{17})$ have no direct influence on the balancing of the DC-link capacitor voltages within the considered control model, since they do not involve any current flow through the neutral point of the converter. They correspond to switching states where the phase terminals are directly connected either to the P or N point of the DC bus or to a zero-output voltage in the case of V_0.

The zero-voltage vector is represented by the switching combination (010101). Although the three possible combinations generate the same AC voltage vector and identical current predictions under ideal conditions, their switching-transition penalties may differ depending on the previous switching state. Therefore, only one combination is retained to reduce the number of evaluated candidates, without guaranteeing the global minimum of the complete cost function.

However, each small voltage vector (SVV) $(V_1, V_2, V_3, V_4, V_5, V_6)$ can be generated by two possible switching combinations, which have opposite effects on DC-link voltage balancing. For example, for vector V_6, the combinations are Comb1 = (110111) and Comb2 = (010001).

To illustrate their effect on neutral-point balancing, we calculate the current i_{zg}:

For Comb1:

$$i_{\mathrm{zg}} = i_{\mathrm{bi}} \tag{69}$$

For Comb2:

$$i_{\mathrm{zg}} = i_{\mathrm{ai}} + i_{\mathrm{ci}} \tag{70}$$

In a balanced three-phase system, we have:

$$i_{\mathrm{ai}} + i_{\mathrm{bi}} + i_{\mathrm{ci}} = 0 \tag{71}$$

Therefore, the two combinations affect the neutral point Z in opposite ways.

To reduce the number of iterations of the FCS-MPC algorithm, a condition on the capacitor voltages V_{c1} and V_{c2} is introduced in order to select the most appropriate combination to be tested for the vectors $(V_1, V_2, V_3, V_4, V_5, V_6)$ during Phase 2.

After applying this condition, the number of combinations to be evaluated is reduced to seven, as detailed in Table 3, which significantly reduces the computational burden.

Table 3. Sectors with associated voltage vectors using capacitor voltage conditions.

Sector	Capacitor Voltages	Voltage Vectors
1	$V_{c1} \geq V_{c2}$	$V_0,\ V_{1(110101)}, V_7, V_8, V_{2(111101)}, V_9, V_{10}$
	$V_{c1} < V_{c2}$	$V_0,\ V_{1(010000)}, V_7, V_8, V_{2(010100)}, V_9, V_{10}$
2	$V_{c1} \geq V_{c2}$	$V_0,\ V_{10}, V_{3(011101)}, V_{11}, V_{12}, V_{4(011111)}, V_{13}$
	$V_{c1} < V_{c2}$	$V_0,\ V_{10}, V_{3(000100)}, V_{11}, V_{12}, V_{4(000101)}, V_{13}$
3	$V_{c1} \geq V_{c2}$	$V_0,\ V_{4(011111)}, V_{13}, V_{5(010111)}, V_{14}, V_{15},, V_{16}$
	$V_{c1} < V_{c2}$	$V_0,\ V_{4(000101)}, V_{13}, V_{5(000001)}, V_{14}, V_{15},, V_{16}$
4	$V_{c1} \geq V_{c2}$	$V_0,\ V_{16}, V_{6(110111)}, V_{17}, V_{18}, V_{1(110101)}, V_7$
	$V_{c1} < V_{c2}$	$V_0,\ V_{16}, V_{6(010001)}, V_{17}, V_{18}, V_{1(010000)}, V_7$

The redundant small-vector selection rule is applied under grid-connected power generation conditions, with active power injected into the grid and the q-axis current reference set to zero. Under these conditions, the grid current is approximately aligned with

the grid voltage. However, as indicated by Equations (69)–(71), the effect of each redundant switching state on the neutral-point voltage also depends on the instantaneous phase currents. Therefore, the voltage-based selection rule does not guarantee corrective balancing at every switching instant, and its effectiveness cannot be generalized to arbitrary current polarities and power-flow directions.

The final selection is then based on the minimization of the following cost function:

$$f_{\mathrm{m}} = [i_{\mathrm{s}\alpha}(k+1) - i^{*}_{\mathrm{s}\alpha}(k+1)]^2 + \left[i_{\mathrm{s}\beta}(k+1) - i^{*}_{\mathrm{s}\beta}(k+1)\right]^2 + \lambda_{\mathrm{s}} \sum_{\chi=\mathrm{a,b,c}} \sum_{\mathrm{j}=1,2} \left[S_{\mathrm{m}\chi\mathrm{j}} - S^{\mathrm{op}}_{\mathrm{m}\chi\mathrm{j}}\right]^2 \quad (72)$$

where λ_s represents a weighting coefficient. This function evaluates the deviation between the predicted stator currents and their references while optimizing the switching frequency through the weighting coefficient λ_{s}. This coefficient defines the importance given to the reduction in the switching frequency.

The prediction of the currents $i_{\mathrm{s}\alpha}(k+1)$ and $i_{\mathrm{s}\beta}(k+1)$ is performed using Model (8).

The weighting coefficient λ_{s} is tuned empirically through successive simulations. Starting from a low value, it is gradually increased while monitoring current tracking accuracy and switching frequency. The final value is selected to achieve a suitable compromise between these two objectives. Although analytical or optimization-based tuning methods can also be considered, the empirical approach is adopted in this study due to its simplicity and ease of implementation. Figure 6a illustrates the steps of the algorithm developed on the machine side.

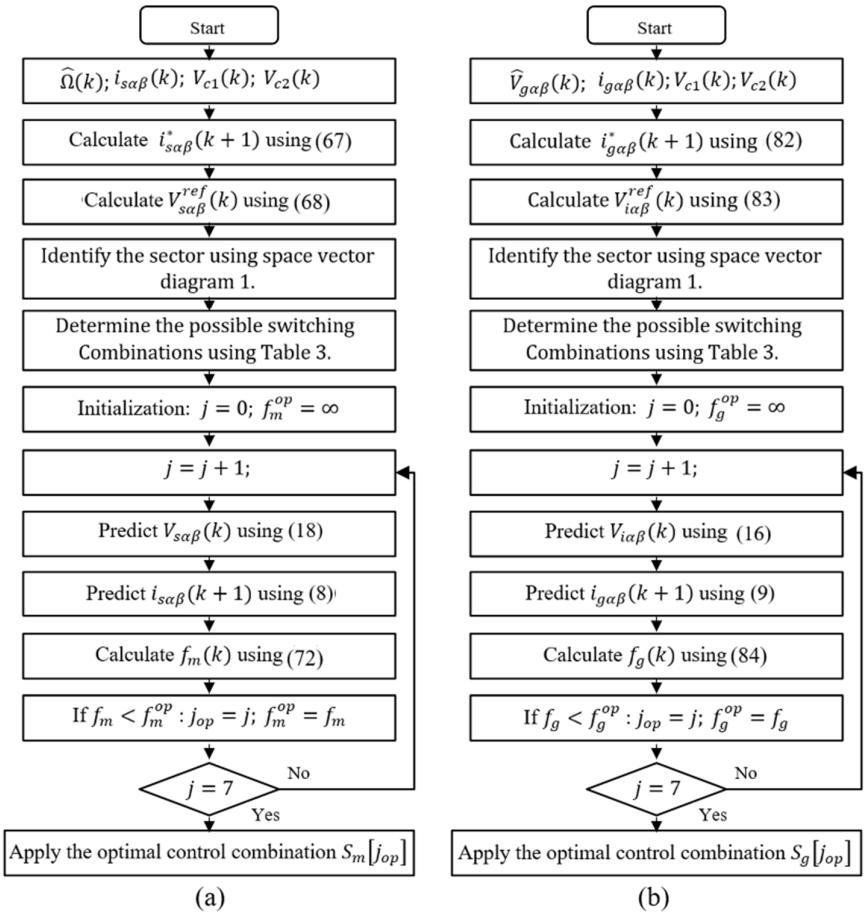


Figure 6. Flowchart of the proposed FCS-MPC: (**a**) MSC; (**b**) GSC.

4.2. Grid-Side Converter Control

The controller of the grid-side converter (GSC) is designed to regulate the DC-bus voltage, balance the voltages of the two capacitors, and control how active and reactive power flows between the grid and the DC bus. It has two loops: an outer loop for the DC-bus voltage and an inner loop for the currents.

4.2.1. Outer Loop

For regulating the DC-bus voltage, an ISMC was used instead of a linear PI controller to improve the system's robustness.

Consider the following sliding surface:

$$S_{\mathrm{dc}} = e_{\mathrm{dc}} + K_3 \int e_{\mathrm{dc}} \tag{73}$$

where $e_{\mathrm{dc}} = V_{\mathrm{dc}}^2 - V_{\mathrm{dc-ref}}^2$ and K_3 is a positive parameter.

The temporal derivative of S_{dc} is expressed by:

$$\dot{S}_{\mathrm{dc}} = \frac{4}{C}\left[P_s - \frac{3}{2}\left(\hat{V}_{\mathrm{gd}} i_{\mathrm{gd}} + \hat{V}_{\mathrm{gq}} i_{\mathrm{gq}}\right)\right] - \frac{dV_{\mathrm{dc-ref}}^2}{dt} + K_3 e_{\mathrm{dc}} \tag{74}$$

Under normal operating conditions, the estimated d-axis grid voltage is assumed to be bounded away from zero, $\left|\hat{V}_{\mathrm{gd}}\right| \geq V_{min} > 0$, to ensure that the current reference remains well defined.

The equivalent control law is expressed as:

$$i_{\mathrm{gd-eq}} = \frac{2}{3\hat{V}_{\mathrm{gd}}}\left[P_{\mathrm{s}} - \frac{3}{2}\hat{V}_{\mathrm{gq}} i_{\mathrm{gq}} + \frac{C}{4}\left(K_3 e_{\mathrm{dc}} - \frac{dV_{\mathrm{dc-ref}}^2}{dt}\right)\right] \tag{75}$$

To analyze stability, we define a Lyapunov function as:

$$V_2 = \frac{1}{2} {S_{\mathrm{dc}}}^2 \tag{76}$$

Its time derivative is then computed as follows:

$$\dot{V}_2 = -\frac{6}{\mathrm{C}} S_{\mathrm{dc}} . V_{\mathrm{gd}} i_{\mathrm{gd-dis}} \tag{77}$$

The following discontinuous control was chosen:

$$i_{\mathrm{gd-dis}} = \frac{CK_4}{6\hat{V}_{\mathrm{gd}}} . \frac{S_{\mathrm{dc}}}{|S_{\mathrm{dc}}| + \varepsilon_2} \tag{78}$$

where K_4 is a positive parameter, and ε_2 is a small positive parameter.

By substituting the expression of the discontinuous control law:

$$\dot{V}_2 = -K_4 \frac{S_{\mathrm{dc}}^2}{|S_{\mathrm{dc}}| + \varepsilon_2} < 0 \tag{79}$$

Therefore, the sliding surface converges to zero under the assumptions of ideal current tracking and accurate state estimation. The global control law is expressed as:

$$i_{\mathrm{gd-ref}} = \frac{2}{3\hat{V}_{\mathrm{gd}}}\left[P_{\mathrm{s}} - \frac{3}{2}\hat{V}_{\mathrm{gq}} i_{\mathrm{gq}} + \frac{C}{4}\left(K_3 e_{\mathrm{dc}} - \frac{dV_{\mathrm{dc-ref}}^2}{dt} + K_4 \frac{S_{\mathrm{dc}}}{|S_{\mathrm{dc}}| + \varepsilon_2}\right)\right] \tag{80}$$

The Lyapunov-based stability analysis of both outer control loops is established under the assumptions of ideal current tracking, accurate state estimation, and operation without actuator saturation. In practical implementation, current-tracking errors, estimation inaccuracies, and parameter uncertainties introduce additional perturbations into the outer-loop dynamics. Therefore, the theoretical convergence results apply under the stated assumptions, while the performance of the complete interconnected control system is assessed through simulation.

4.2.2. Inner Loop

a. Conventional FCS-MPC

The conventional predictive control on the grid side is based on minimizing the following function:

$$f_{c_g} = \left[i_{g\alpha}(k+1) - i^*_{g\alpha}(k+1)\right]^2 + \left[i_{g\beta}(k+1) - i^*_{g\beta}(k+1)\right]^2 + \lambda_{dc}.[V_{c1}(k+1) - V_{c2}(k+1)]^2 + \lambda_{c_g}\sum_{\chi=a,b,c}\sum_{j=1,2}\left[S_{g_{\chi j}} - S^{op}_{g_{\chi j}}\right]^2 \quad (81)$$

The weighting coefficient λ_{c_g} is associated with the switching frequency constraint, while λ_{dc} represents the one related to DC-bus voltage balancing. A high value of λ_{dc} gives greater priority to this secondary constraint, thereby improving voltage balancing. However, this comes at the expense of the accuracy and dynamics of reference current tracking. Therefore, it is crucial to carefully adjust this parameter to limit the imbalance to less than 2%.

A fourth-order Lagrange formula is employed to estimate the reference currents as follows:

$$i^*_{g\alpha\beta}(k+1) = 4i^*_{g\alpha\beta}(k) - 6i^*_{g\alpha\beta}(k-1) + 4i^*_{g\alpha\beta}(k-2) - i^*_{g\alpha\beta}(k-3) \quad (82)$$

The selection of the optimal control combination for the next time step is carried out by systematically exploring all 27 possible configurations. At each iteration, the currents $i_{g\alpha}(k+1)$ and $i_{g\beta}(k+1)$, as well as the voltages $V_{c1}(k+1)$ and $V_{c2}(k+1)$, are predicted using Equations (9), (12) and (13). The detailed process of the conventional FCS-MPC applied to the grid is illustrated in Figure 4b.

b. Proposed FCS-MPC

Following the same approach used on the MSC to design the grid-side regulator, the cost function minimization algorithm is organized into two main phases.

- **Step 1: Sector identification**

The first phase aims to identify the sector containing the optimal control to be applied at the next time step. From the discrete Model (9), the reference voltage at the inverter output is then computed according to the following equations.

$$\begin{cases} V^{ref}_{i\alpha}(k) = \frac{L_f}{T_s} i^*_{g\alpha}(k+1) + \left(R_f - \frac{L_f}{T_s}\right) i_{g\alpha}(k) + \hat{V}_{g\alpha}(k) \\ V^{ref}_{i\beta}(k) = \frac{L_f}{T_s} i^*_{g\beta}(k+1) + \left(R_f - \frac{L_f}{T_s}\right) i_{g\beta}(k) + \hat{V}_{g\beta}(k) \end{cases} \quad (83)$$

Based on the sign of the components $V^{ref}_{i\alpha}$ and $V^{ref}_{i\beta}$ and using the space vector diagram, the corresponding sector is identified. This phase reduces the number of control combinations to be checked in the cost function minimization phase to 11, thereby decreasing the computational load of predictive control.

- **Step 2: Selection of the optimal combination for the GSC**

Phase 2 aims to determine the optimal combination within the sector identified in the previous step. As in Phase 2 of MSC control, the condition given in Table 3 is first used to define the set of candidate combinations to be tested. These combinations are then evaluated in order to minimize the following cost function:

$$f_g = \left[i_{g\alpha}(k+1) - i^*_{g\alpha}(k+1)\right]^2 + \left[i_{g\beta}(k+1) - i^*_{g\beta}(k+1)\right]^2 + \lambda_g \sum_{\chi=a,b,c}\sum_{j=1,2}\left[S_{g_{\chi j}} - S^{op}_{g_{\chi j}}\right]^2 \quad (84)$$

The currents $i_{g\alpha}(k+1)$ and $i_{g\beta}(k+1)$ are predicted using Equation (9), and λ_g is the weighting factor, with higher values giving greater priority to reducing switching losses by limiting switch state variations.

The cost function f_g incorporates two main objectives as well as a secondary constraint aimed at minimizing the switching frequency. However, the constraint of DC-bus voltage balancing is not explicitly integrated into it. Instead, it is indirectly considered by applying a condition on the voltages V_{c1} and V_{c2}, allowing the selection, from the outset, of the most appropriate control combination among the two possible options for the same voltage vector. Figure 6b illustrates the proposed FCS-MPC algorithm for grid-side control by describing the steps of the optimal control selection process. The proposed control scheme is illustrated in Figure 7.

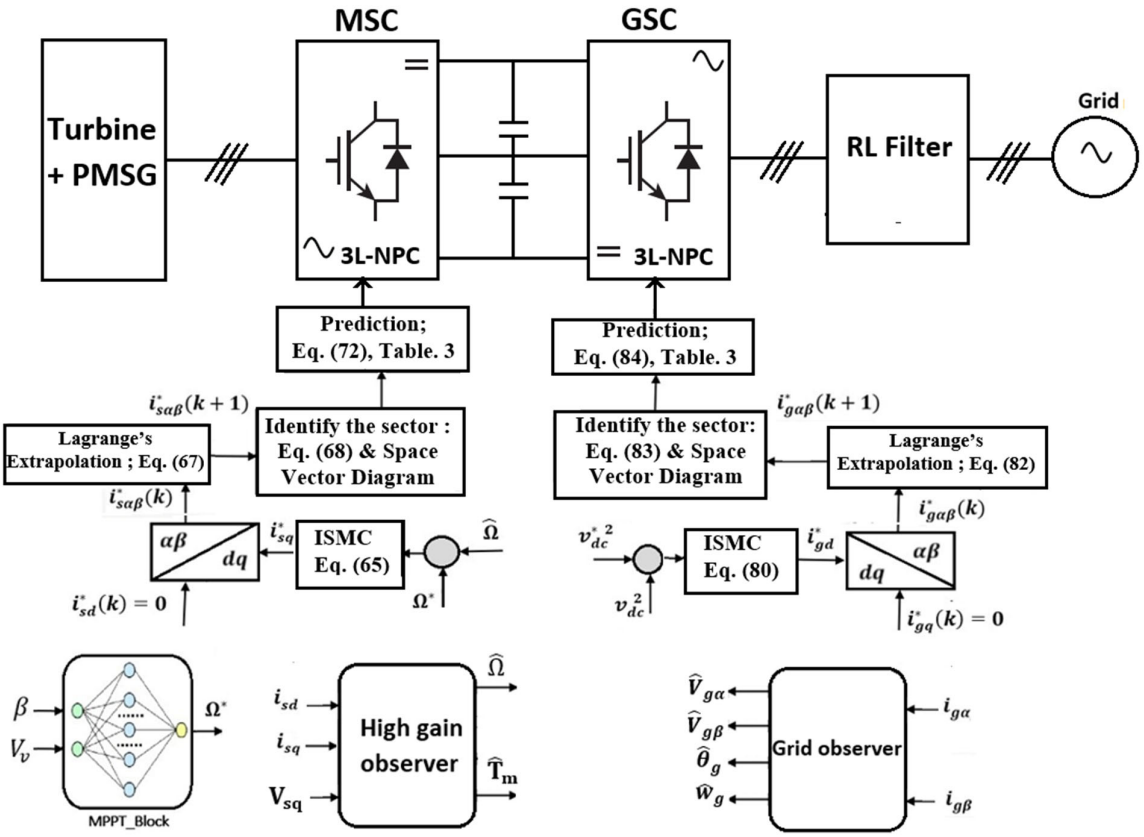


Figure 7. The control scheme of controller for WECS. The superscript * denotes reference values.

5. Simulation and PIL Results

In this section, the proposed control strategy is evaluated through Processor-in-the-Loop (PIL) simulations using MATLAB/Simulink and the TI LAUNCHXL-F28379D development board. The PMSG-based WECS is modeled in MATLAB/Simulink, while the control algorithm is executed on the Delfino F28379D microcontroller (Texas Instruments, Dallas, TX, USA), as shown in Figure 8. A fixed-step solver with a sampling period of 10 µs is used. The WECS and controller parameters are given in Tables 4 and 5, respectively. The embedded code is generated using the Embedded Coder Support Package for Texas Instruments C2000 and deployed on the target microcontroller. Communication between the host computer and the target board is performed via a serial USB (COM port) interface, enabling data exchange required for Simulink-based execution. The experimental PIL setup is shown in Figure 9. The system operates in a closed-loop configuration, where the control algorithm runs directly on the hardware platform while the plant model remains implemented in MATLAB/Simulink. At each sampling instant T_s, input and

output signals are exchanged between the host environment and the target device. The proposed control strategy is evaluated under different operating conditions of the WECS.

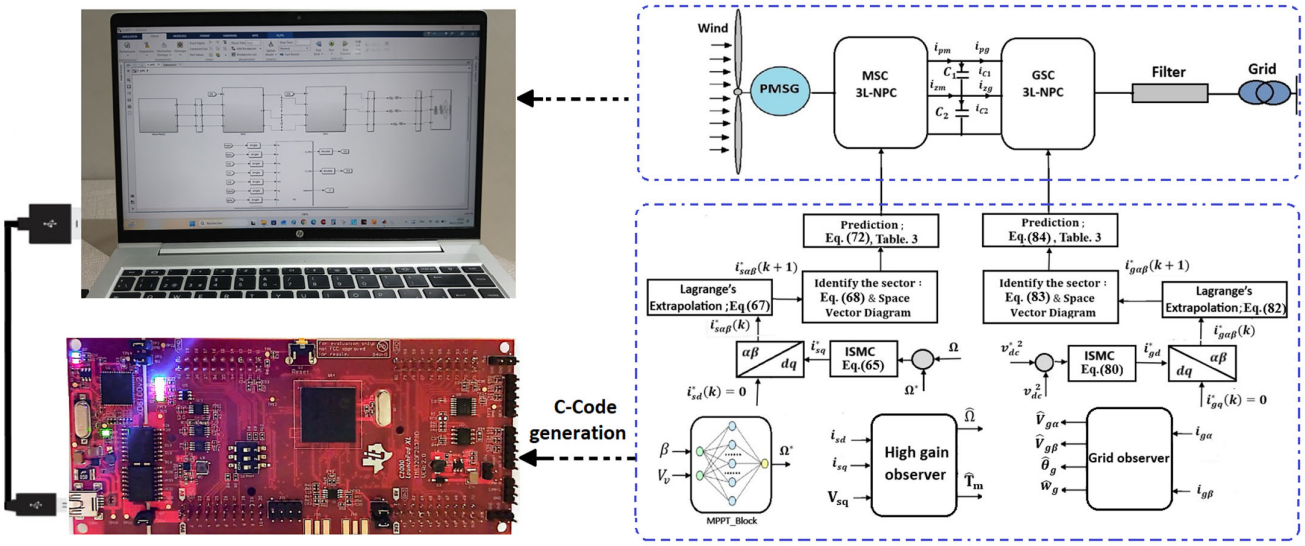


Figure 8. PIL test of the proposed FCS-MPC.



Figure 9. PIL testing of the proposed approach using the LAUNCHXL-F28379D microcontroller.

Table 4. System parameters.

Parameter	Value	Parameter	Value
R_s (mΩ)	5	p	160
L_d (mH)	0.6	J (kg. m^2)	50,000
L_q (mH)	0.6	C_1 and C_2 (mF)	40
Radius R (m)	85	L_f (mH)	1.2
Φ_f (wb)	15.34	R_f (mΩ)	0.1
Power Generator P_n (MW)	10	Grid line-to-line RMS voltage V_g (V)	3300

Table 5. Controller parameters.

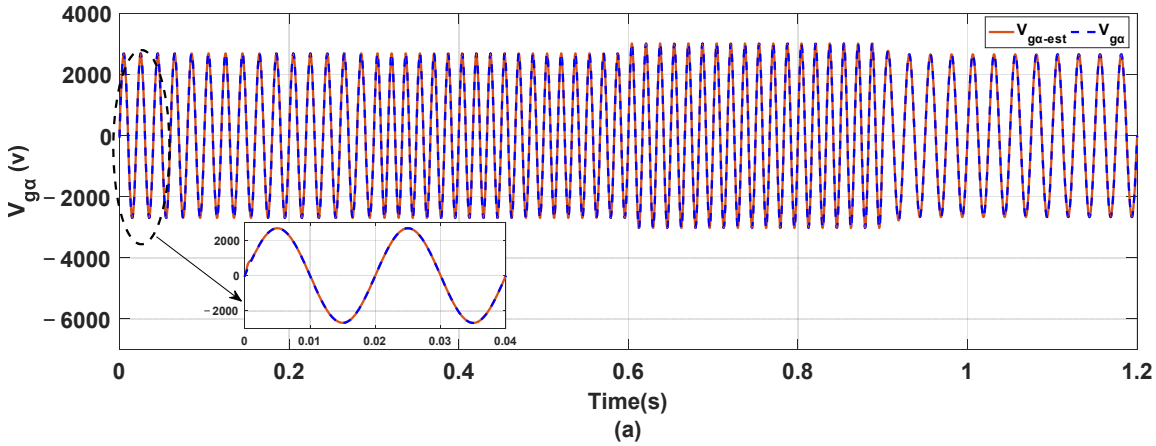
	Parameter	Value
Speed control	K_1	2000
	K_2	1×10^{-3}
	ε_1	1×10^{-3}
Current control—MSC	$\lambda_{c-s};\ \lambda_s$	3
DC-link voltage	K_3	50
	K_4	200
	ε_2	1×10^{-3}
Current control—GSC	$\lambda_{c-g};\lambda_g$	3
Grid observer	θ	8000
	b	0.33

5.1. Test of Grid Observer

5.1.1. Observer Response to Abrupt Grid Frequency and Voltage Amplitude Changes

The objective of this section is to validate the behavior of the network observer. For this purpose, a PIL simulation is performed. Initially, the network operates under nominal conditions. At $t = 0.3$ s, it undergoes a 10 Hz increase in frequency. Then, at $t = 0.6$ s, an increase in amplitude is applied. Finally, at $t = 0.9$ s, the network experiences a simultaneous decrease in both frequency and amplitude.

Figure 10 shows the response of the proposed network observer under both nominal and disturbed grid operating conditions. For the grid voltages in the α and β reference frame, it can be observed that the estimated values closely track the actual values with an almost negligible response time. Similarly, the grid angular frequency, w_g, is accurately estimated despite the disturbances applied to the grid, with a response time of approximately 0.001 s. The phase angle, θ_g, also exhibits excellent tracking performance throughout the entire operating period. These results demonstrate that the proposed observer can accurately estimate the grid parameters using only direct current measurements without requiring additional sensors. Furthermore, the observer responds rapidly to variations in grid frequency and voltage amplitude, confirming its excellent dynamic performance under disturbed operating conditions. These abrupt disturbances are not directly covered by the theoretical convergence assumptions. However, the simulation results show that the observer rapidly recovers accurate estimation after these disturbances.



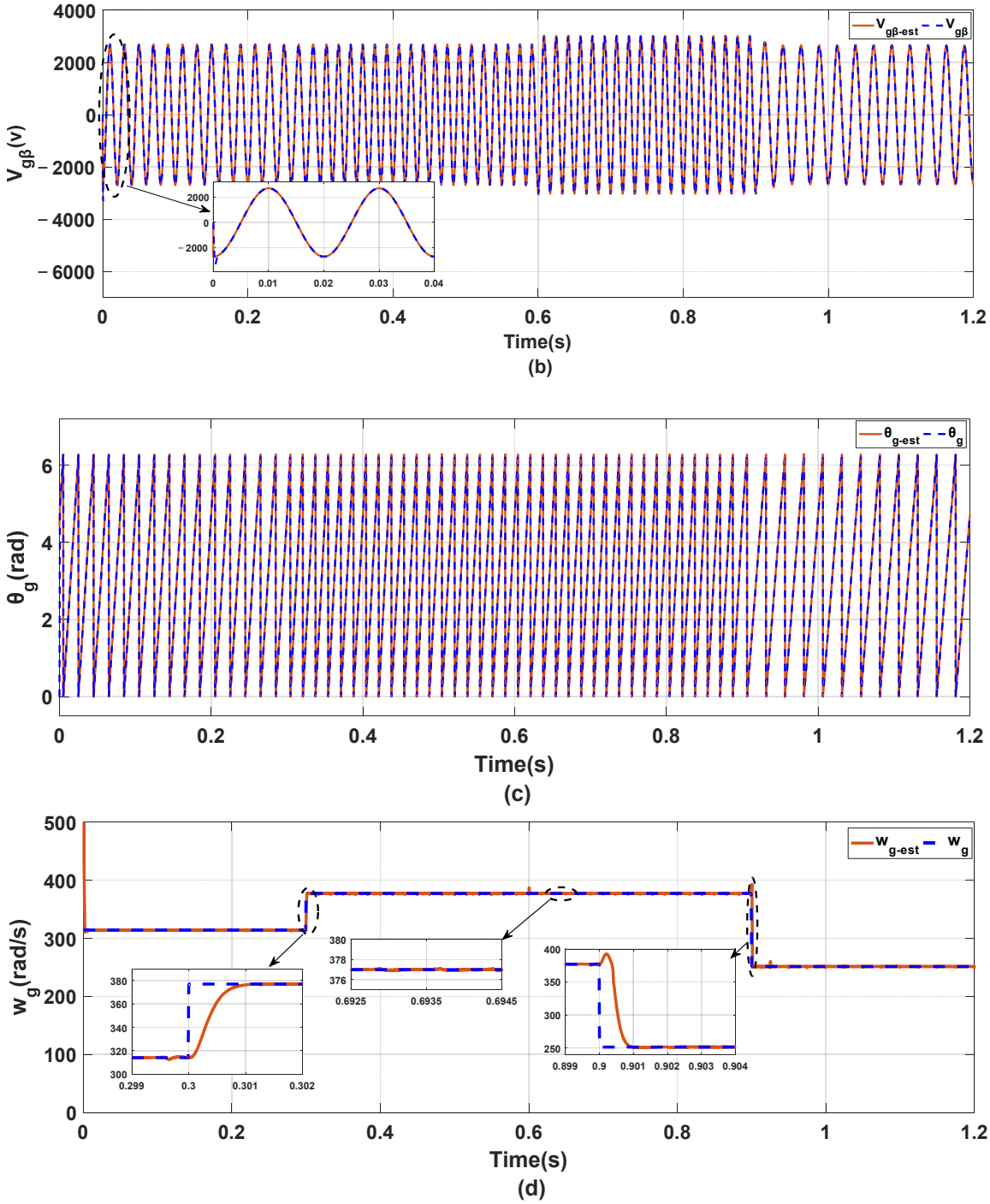


Figure 10. The response of the network observer: (**a**) Voltage $V_{g\alpha}$; (**b**) voltage $V_{g\beta}$; (**c**) electrical angle; (**d**) grid pulsation.

5.1.2. Observer Performance Under Bounded Frequency Variations

This test aims to evaluate the observer's ability to estimate the grid variables during a frequency ramp, while maintaining the grid voltage amplitude at its nominal value. The grid frequency varies according to the following profile:

$$f_g(t) = \begin{cases} 50\ \text{Hz};\ \ 0 \le t < 0.5\ \text{s} \\ 20t + 40\ \text{Hz};\ 0.5\ \text{s} \le t \le 1\ \text{s} \\ 60\ \text{Hz},\ \ t > 1\ \text{s} \end{cases} \quad (85)$$

Figure 11 presents the performance of the grid-side observer under a frequency ramp from 50 to 60 Hz. After an initial transient phase, the estimation errors of the grid voltage components $V_{g\alpha}$ and $V_{g\beta}$ remain within approximately ± 10 V. The estimated electrical angle θ_g closely follows its actual value, with a nearly zero estimation error after convergence. At startup, the estimated grid angular frequency w_g exhibits a transient peak of approximately 2650 rad/s before rapidly converging to its reference value of 314.16 rad/s. It then accurately tracks the frequency ramp up to 376.99 rad/s, with an estimation error limited to approximately ± 0.4 rad/s. These results show that the observer maintains good estimation accuracy during grid frequency variations.

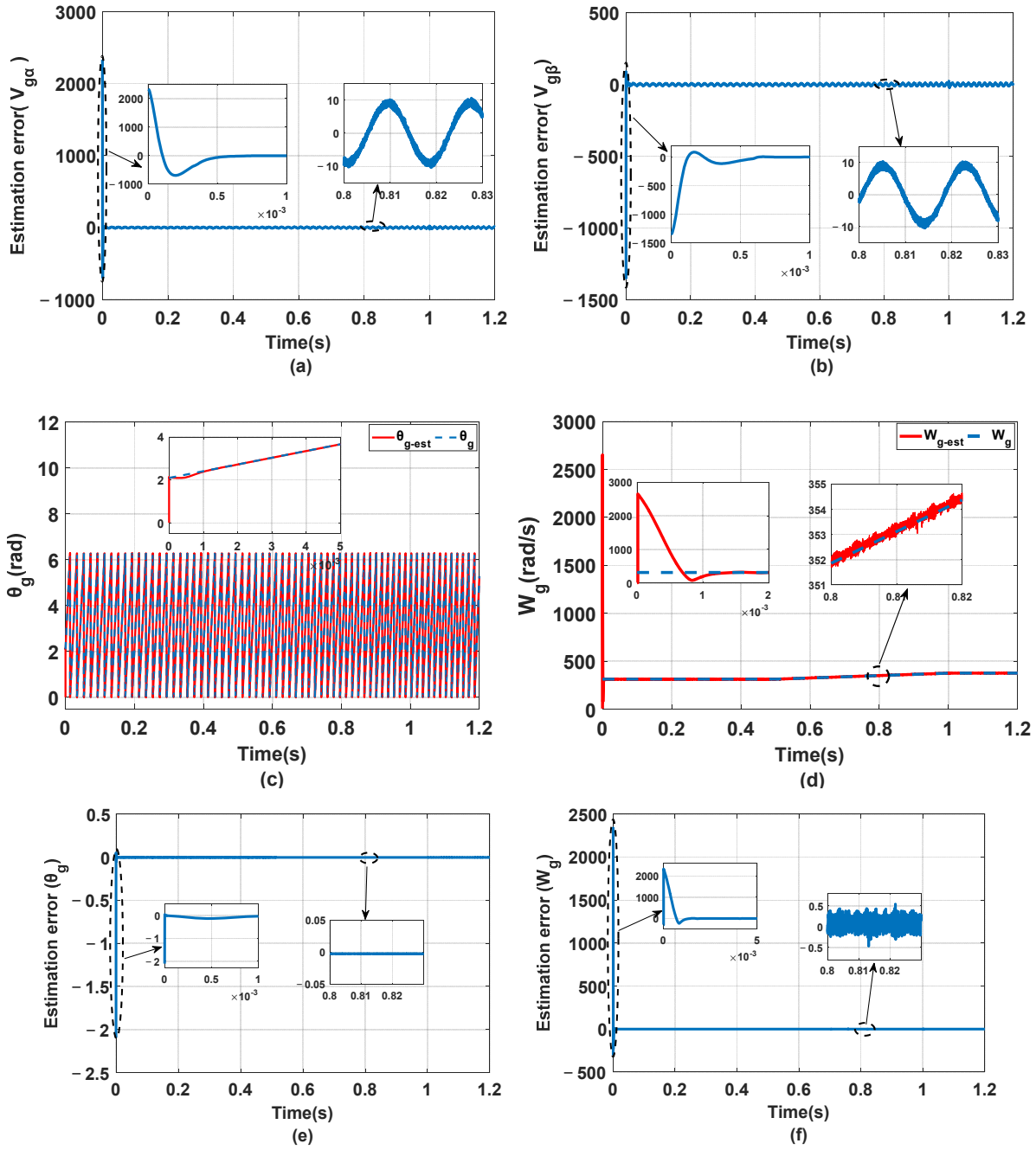


Figure 11. Grid-side observer performance under a frequency ramp: (**a**,**b**) Voltage estimation errors; (**c**,**d**) electrical angle and angular frequency tracking; (**e**,**f**) corresponding estimation errors.

https://doi.org/10.3390/en19215378

5.1.3. Observer Robustness Test Under Measurement Noise

High-gain observers are generally sensitive to measurement noise, whose amplification can introduce oscillations in the estimated variables and affect estimation accuracy. This test aims to evaluate the observer's sensitivity to measurement noise. For this purpose, uniformly distributed random noise with an amplitude of ± 10 A, generated using the Uniform Random Number block in MATLAB/Simulink, is added to the measured grid currents $i_{g\alpha}$ and $i_{g\beta}$, as shown in Figure 12. Initially, the observer gain is set to $\theta = 8000$.

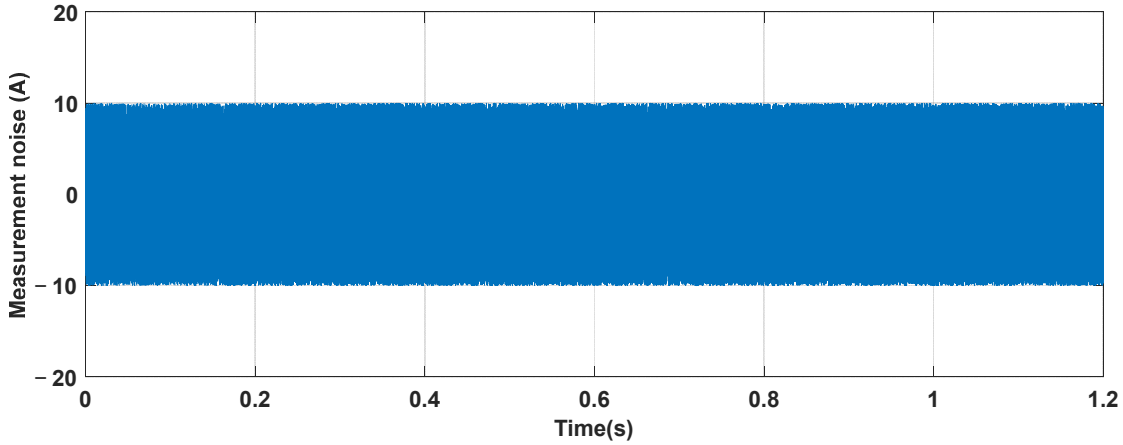
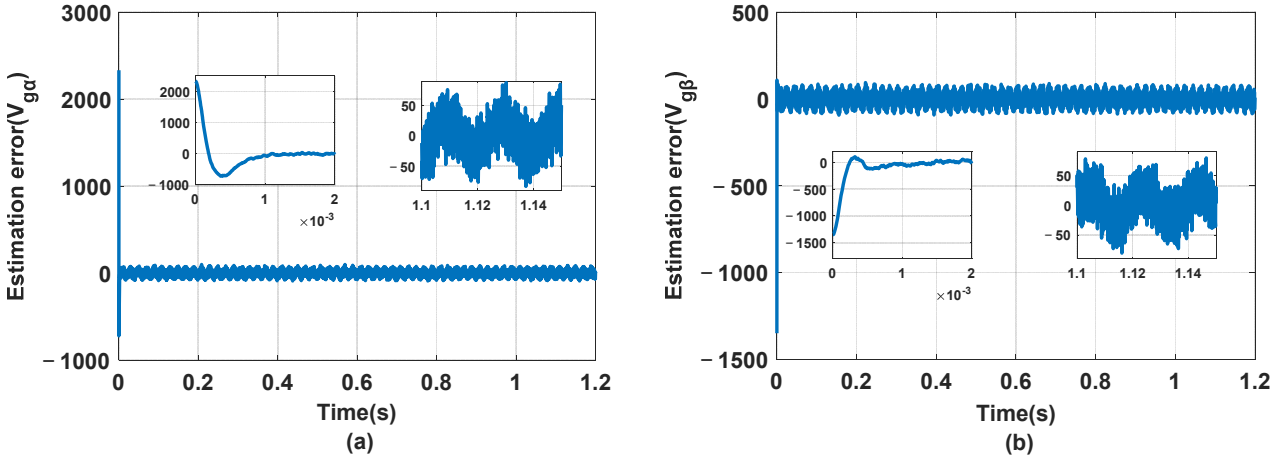


Figure 12. Measurement noise.

Figure 13 presents the estimation results obtained in the presence of uniform measurement noise of $\pm 10\ A$, with the observer gain set to $\theta = 8000$. After an initial transient period, the estimation errors of the grid voltages $V_{g\alpha}$ and $V_{g\beta}$ oscillate around zero, with approximate amplitudes of $\pm 60\ V$. The estimated electrical angle remains close to its actual value, with small fluctuations in the estimation error. The estimated angular frequency exhibits an initial transient peak and subsequently oscillates around its nominal value of 314.16 rad/s, with an estimation error reaching approximately $\pm 50\ rad/s$. These results indicate that the observer maintains its tracking capability in the presence of measurement noise, although the estimation accuracy is affected by the observed oscillations.



https://doi.org/10.3390/en19215378

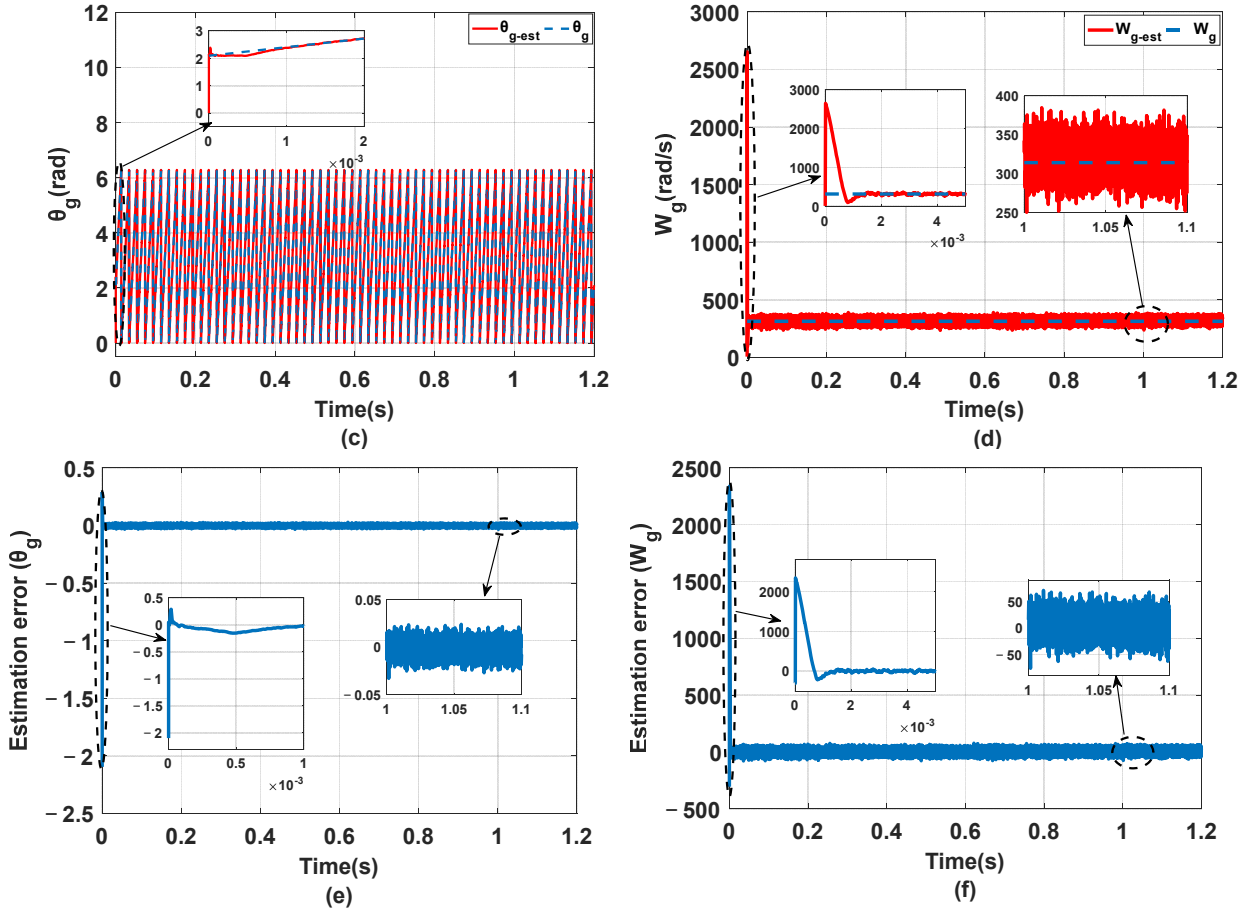


Figure 13. Grid-side observer performance under measurement noise: (**a**,**b**) Voltage estimation errors; (**c**,**d**) electrical angle and angular frequency tracking; (**e**,**f**) corresponding estimation errors.

To further investigate the influence of the observer gain on estimation accuracy under measurement noise, three gain values are considered: $\theta = 8000, 6000$ and 4000. The same noise realization and simulation conditions are maintained, with only the observer gain varied. The performance is evaluated using the root mean square error (RMSE) and mean absolute error (MAE) for the estimated grid voltages, electrical angle, and angular frequency. Both indicators are calculated over the interval from 0.1 to 1.2 s, after the initial transient response.

Table 6 summarizes the RMSE and MAE values obtained for the three observer gains under the same measurement noise conditions. The results show that increasing the gain from 4000 to 8000 reduces the voltage estimation RMSE from 63.8243 to 26.6714 V for $V_{g\alpha}$ and from 63.8116 to 26.5546 V for $V_{g\beta}$. However, the lowest RMSE values for the electrical angle and angular frequency are obtained with $\theta = 6000$, reaching 0.0065 rad and 10.8549 rad/s, respectively. These results indicate that the influence of the observer gain on estimation accuracy depends on the estimated variable, with no single gain providing the lowest errors for all variables.

Table 6. RMSE and MAE of the estimated grid variables under measurement noise for different observer gains.

		Gain Observer		
		$\boldsymbol{\theta = 8000}$	$\boldsymbol{\theta = 6000}$	$\boldsymbol{\theta = 4000}$
$V_{g\alpha}$	RMSE (V)	26.6714	32.6562	63.8243

	MAE (V)	21.6767	28.2194	57.2383
$V_{g\beta}$	RMSE (V)	26.5546	32.6008	63.8116
	MAE (V)	21.5293	28.1874	57.2588
θ_g	RMSE (rad)	0.0077	0.0065	0.0131
	MAE (rad)	0.0062	0.0053	0.0129
w_g	RMSE (rad/s)	19.2034	10.8549	19.9114
	MAE (rad/s)	15.4105	8.7567	19.6459

5.2. Test of the Control Techniques

To ensure a fair comparison between the conventional FCS-MPC and the proposed reduced-search FCS-MPC, both control strategies are evaluated under identical operating conditions. The same outer speed and DC-link voltage control loops, as well as the same observers, are maintained for both methods.

5.2.1. Step Change in Wind Speed

The proposed control strategy was evaluated using a wind profile subjected to sudden step changes in order to evaluate the system's response during both transient and steady-state regimes. For this purpose, a wind profile as shown in Figure 14, with speeds varying between 6 m/s and 11 m/s, was employed. Initially, the wind speed is set to 8 m/s for the first 0.5 s, followed by step changes applied every 0.5 s.

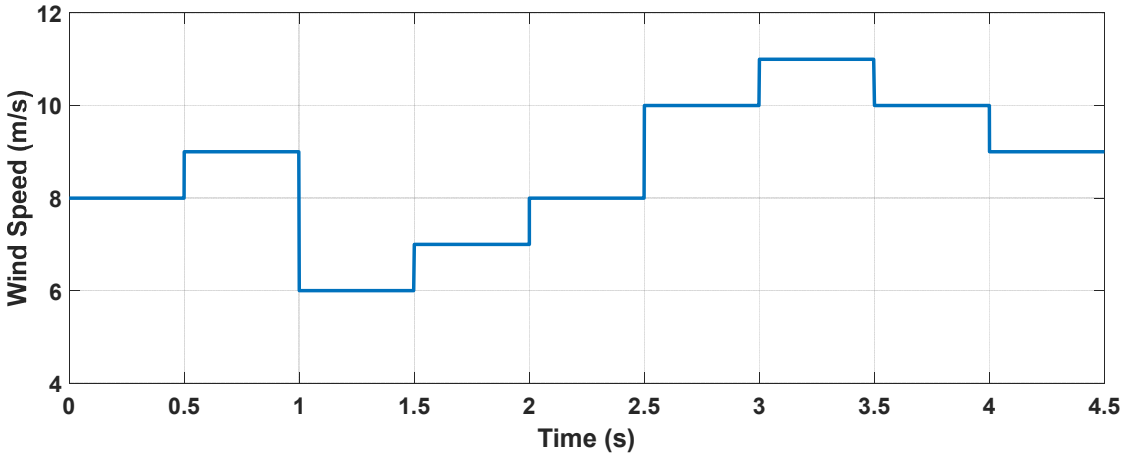


Figure 14. Wind speed.

Figure 15 shows that both strategies achieve satisfactory tracking of the reference speed provided by the MPPT block. However, the conventional method exhibits more pronounced steady-state fluctuations, with speed variations of approximately 0.950 to 0.952 rad/s, compared with 0.951 to 0.9515 rad/s for the proposed method. In contrast, the proposed strategy provides a more stable response with reduced speed oscillations.

These differences may be attributed to the switching-state selection strategy adopted in the proposed FCS-MPC, which combines a reduced search space with capacitor-voltage-based redundant-state selection. Although both methods employ identical outer control loops, observers, weighting coefficients, and sampling periods, they may select different switching combinations, resulting in different current-tracking behavior and speed fluctuations. Furthermore, the proposed method reduces the number of evaluated switching combinations from 27 to 7, thereby decreasing the computational burden without changing the sampling period.

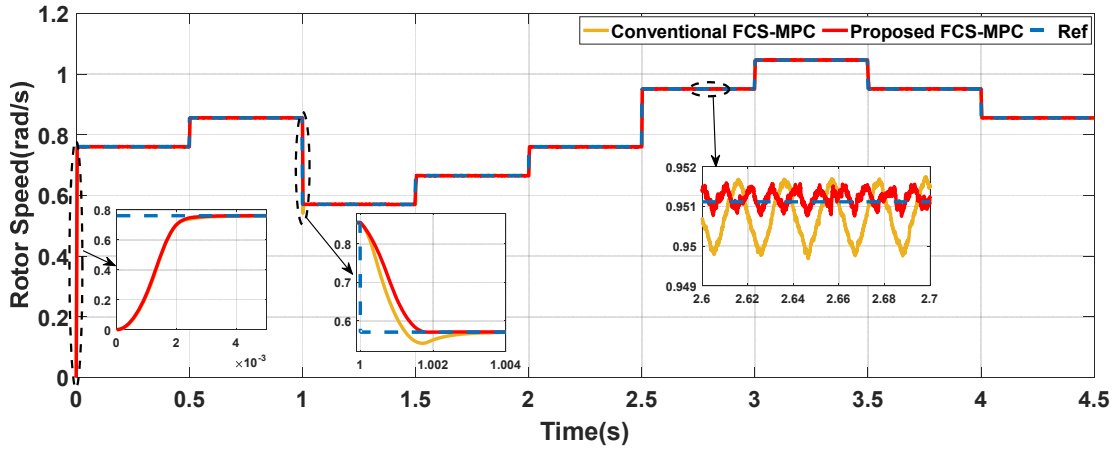


Figure 15. Rotor speed response to step changes in wind speed.

The two control approaches used for regulating the DC-link voltage exhibit nearly similar response times, as shown in Figure 16. However, the conventional method presents larger steady-state voltage fluctuations, reaching approximately 3 V peak-to-peak, compared with about 1 V for the proposed strategy.

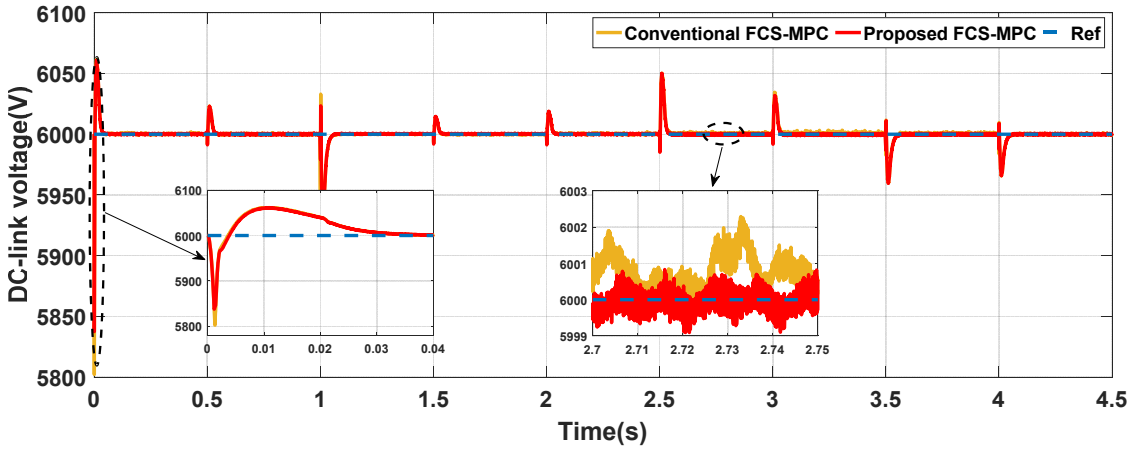


Figure 16. DC-bus voltage under nominal operating conditions.

Figure 17 illustrates the DC-link capacitor voltages, V_{c1} and V_{c2}, obtained using both methods. As highlighted in the enlarged view, at a wind speed of 6 m/s, the capacitor voltages remain close to their nominal value of 3000 V, with a voltage difference of approximately ± 3 V for the conventional method and ± 1 V for the proposed method. The proposed method therefore provides better voltage balancing under the investigated conditions. These results indicate that the switching combinations selected within the sector identified in Phase 1 contribute to capacitor-voltage balancing, even though this constraint is not explicitly included in the cost function.

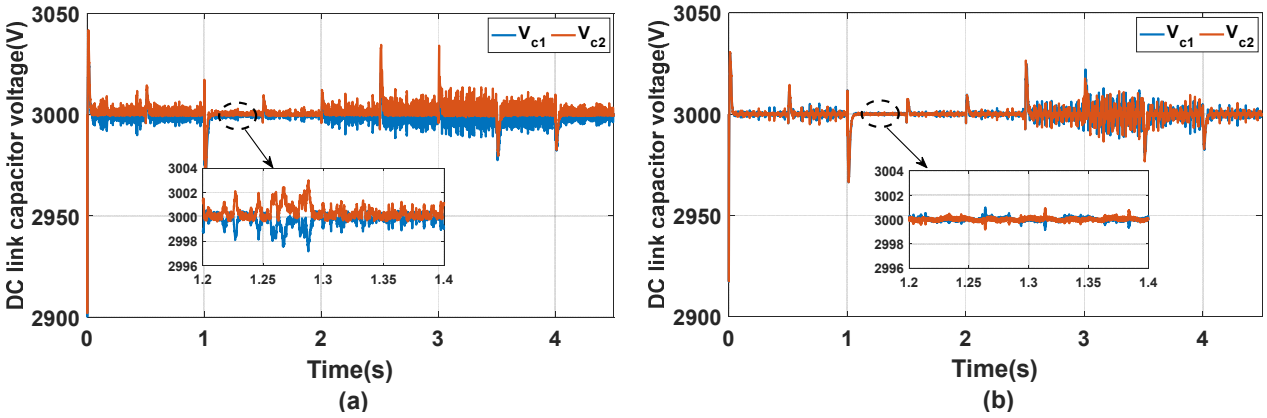


Figure 17. DC-bus capacitor voltages: (**a**) Conventional FCS-MPC, (**b**) proposed FCS-MPC.

The grid-current THD was calculated using the FFT Analysis tool in MATLAB/Simulink powergui, with a fundamental frequency of 50 Hz. The analysis was performed over three fundamental cycles (0.06 s). The spectra are displayed up to 1 kHz, while the THD calculation includes frequency components up to the Nyquist frequency. The same FFT settings were used for both control methods under nominal conditions and parametric uncertainties.

Figure 18 shows that both methods achieve similar grid-current THD values of 0.64% for conventional FCS-MPC and 0.62% for the proposed FCS-MPC. Furthermore, the injected current exhibits a nearly sinusoidal waveform and remains approximately in phase with the grid voltage, indicating good power quality and a near-unity power factor under nominal operating conditions.

To compare the computational burden of the conventional and proposed FCS-MPC methods, PIL execution profiling was performed under identical conditions, using the same simulation time, solver, sampling period, and target hardware. The measured execution times are reported in Table 7. The proposed method reduces the total measured execution time from 46.05 s to 18.40 s, corresponding to a reduction of approximately 60%. This improvement is mainly achieved by reducing the number of evaluated switching combinations from 27 to 7 per sampling period. However, the maximum execution time of the proposed method (52.685 µs) exceeds the simulation sampling period of 10 µs. Therefore, these results do not establish real-time feasibility at this sampling rate. The PIL profiling is used here to compare the computational requirements of the two control strategies rather than to demonstrate complete real-time implementation feasibility.

Table 7. Computational time comparison between conventional FCS-MPC and proposed FCS-MPC.

Performance Metric	Conventional FCS-MPC	Proposed FCS-MPC	Improvement
Average Execution Time (ns)	102,330	40,883	2.50 faster
Maximum Execution Time (ns)	103,135	52,685	1.96 faster
Total Execution Time (s)	46.05	18.40	60% reduction

To investigate whether a longer sampling period could satisfy the execution-time constraint, additional tests were performed under identical operating conditions with sampling periods of 10, 30, and 60 µs. The influence of the sampling period on control performance was evaluated using the root mean square error (RMSE), the integral of time-weighted absolute error (ITAE), and the grid-current total harmonic distortion (THD). The results are summarized in Table 8.

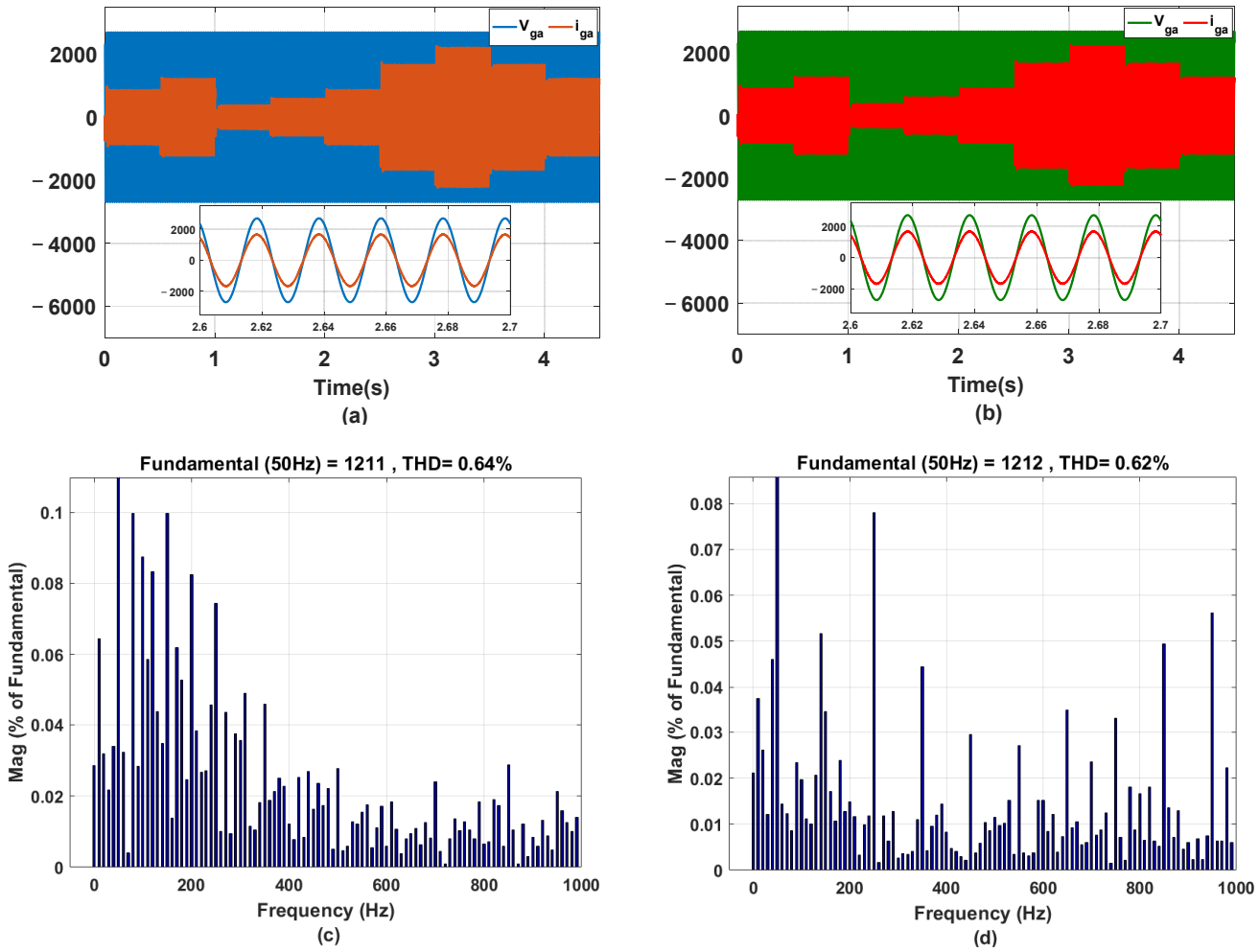


Figure 18. Injected current and grid current THD: (**a**,**c**) Conventional FCS-MPC, (**b**,**d**) proposed FCS-MPC.

Table 8. Effect of the sampling period on control performance and real-time execution feasibility.

		$T_s = 10\ \mu s$	$T_s = 30\ \mu s$	$T_s = 60\ \mu s$
Ω	RMSE (rad/s)	0.012	0.0123	0.013
	ITAE (rad. s)	0.0043	0.0113	0.0267
$i_{s\alpha}$	RMSE (A)	248.7079	278.0161	334.6061
	ITAE ($A.s^2$)	297.3491	921.2267	1697.6
$i_{s\beta}$	RMSE (A)	48.1592	115.7683	216.8327
	ITAE ($A.s^2$)	212.94	657.1628	1290.8892
V_{dc}	RMSE (V)	6.9909	7.1208	7.4384
	ITAE ($V.s^2$)	14.8857	18.0969	25.1906
Neutral point	RMSE (V)	2.8829	2.9478	3.4046
	ITAE ($V.s^2$)	15.1445	17.0018	22.8012
$i_{g\alpha}$	RMSE (A)	5.6672	15.7610	31.2896
	ITAE ($A.s^2$)	43.4956	128.2631	253.9735
$i_{g\beta}$	RMSE (A)	6.2286	16.0297	31.6248
	ITAE ($A.s^2$)	43.6028	128.7372	255.1628
i_g	THD (%)	0.62	1.7	3.28
Average execution time (µs)		40.883	40.890	40.902

Maximum execution time (µs)	52.685	52.765	52.795
$\frac{T_{exec,max}}{T_s}.100(\%)$	526.85	175.88	87.99
Measured execution-time constraint satisfied	No	No	Yes

As shown in Table 8, the average execution time remains close to 40.9 µs, while the maximum execution time is approximately 52.8 µs for all three sampling periods. The execution-time constraint is not satisfied at 10 µs and 30 µs. However, at 60 µs, the maximum measured execution time is lower than the sampling period, indicating that the timing constraint is satisfied under the tested conditions.

Increasing the sampling period leads to higher current-tracking errors, as indicated by the RMSE and ITAE values. In contrast, the speed and DC-link voltage RMSE increase only slightly, by 8.33% and 6.40%, respectively. The grid-current THD increases from 0.62% to 3.28%. These results show that a sampling period of 60 µs satisfies the measured timing constraint, although some degradation in control performance is observed.

The calculation of the average switching frequency of both converters, on the machine side and the grid side, is carried out to highlight the impact of the optimization on switching losses. The average switching frequency is defined as:

$$f_{sw}(Hz) = \frac{N_{com}}{12.T} \quad (86)$$

where N_{com} denotes the total number of commutations of the converter, and T is the observation time.

Table 9 presents a comparative study between the proposed approach and the conventional method for different wind speeds, where the reduction in the switching frequency is calculated as:

$$Reduction\ (\%) = 100.\frac{f_{sw}^{C-MPC} - f_{sw}^{P-MPC}}{f_{sw}^{C-MPC}} \quad (87)$$

The proposed method systematically reduces the switching frequency for both converters under the investigated operating conditions, which may contribute to lower switching losses and a potential improvement in IGBT reliability. The effect is particularly significant on the GSC side (23.51% to 28.82), especially at intermediate wind speeds, whereas on the MSC side, the reduction is more moderate, ranging from 2.57% to 16.22%, with the maximum effect at low wind speeds gradually decreasing as the speed increases.

In comparison, the conventional FCS-MPC, by exhaustively exploring 27 switching combinations, produces higher switching frequencies than the proposed approach, which may increase switching losses and thermal and electrical stress on the IGBTs, potentially affecting their lifetime. These observations indicate that the proposed method effectively reduces switching frequency under the investigated operating conditions.

Table 9. Comparative analysis of average switching frequency (Hz).

	Average Switching Frequency (Hz)					
	Machine-Side Converter			**Grid-Side Converter**		
Wind Speed (m/s)	**Conventional FCS-MPC**	**Proposed FCS-MPC**	**Reduction (%)**	**Conventional FCS-MPC**	**Proposed FCS-MPC**	**Reduction (%)**
8	22,023	18,450	16.22	18,828	14,400	23.51
9	20,992	18,525	11.75	19,225	13,990	27.23
10	19,738	18,540	6.06	19,528	13,900	28.82
11	18,355	17,882	2.57	19,347	14,155	26.83

5.2.2. Stochastic Wind Velocity Variation with System Parameters Uncertainties

To further test the robustness of the proposed method, a simulation was carried out under stochastic wind variations and uncertainties in the WECS parameters. A realistic wind profile, shown in Figure 19, was used. Additionally, the WECS parameters were subjected to uncertainties, including a 50% increase in the PMSG parameters (J, R_s, L_s) and the filter (R_f, L_f), while the capacitance of the capacitor C_1 exhibited a −50% uncertainty. These uncertainties were applied only to the system model, while the controller parameters were kept at their nominal values.

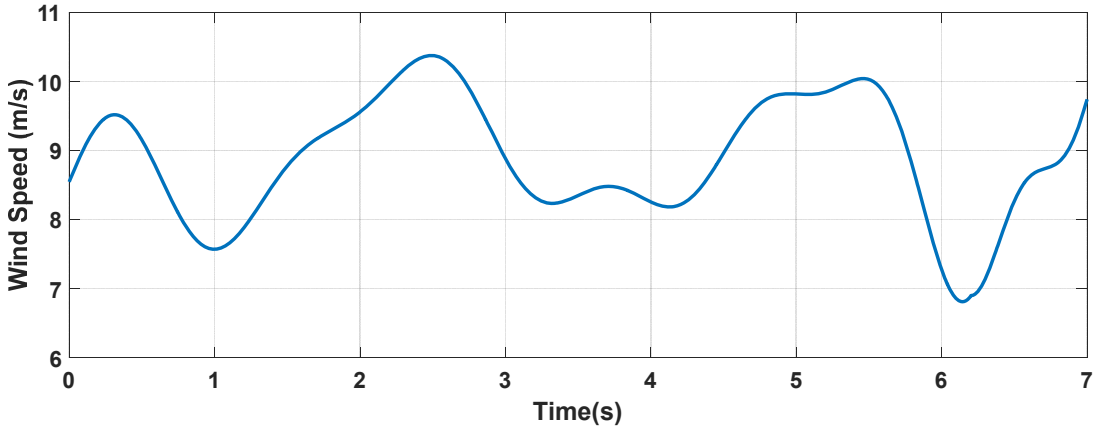


Figure 19. Stochastic wind speed.

Figure 20 shows the response of the PMSG speed control loop obtained with the two control methods under parametric uncertainties. Both methods follow the reference generated by the MPPT block. However, the conventional FCS-MPC exhibits more pronounced speed oscillations, with deviations of approximately ± 0.0018 rad/s around the reference in the enlarged view. In contrast, the proposed method shows smaller fluctuations and more accurate reference tracking under the investigated conditions.

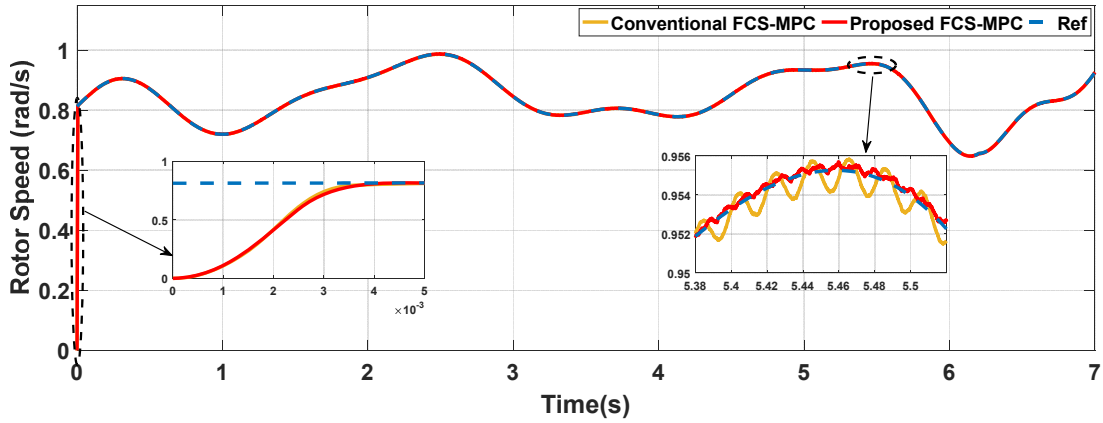


Figure 20. Rotor speed.

Figure 21 compares the DC-bus voltage obtained using the two control methods. The conventional controller shows a steady-state error of about 10 V, along with significant oscillations around 6010 V, whereas the proposed approach provides a more stable response and keeps the voltage much closer to its reference value.

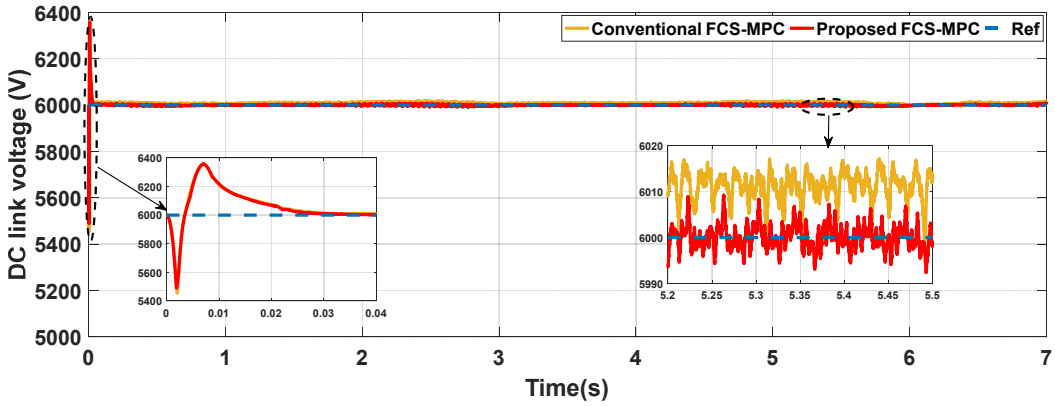


Figure 21. DC-bus voltage.

The DC-link capacitor voltage balancing performance under parameter uncertainties and stochastic wind variations is illustrated in Figure 22. The conventional FCS-MPC exhibits a noticeable difference between the two capacitor voltages, V_{c1} and V_{c2}, around the 3000 V reference. In contrast, the proposed FCS-MPC maintains the two capacitor voltages closer to each other and to the reference value. As shown in Figure 22c, the neutral-point voltage fluctuates approximately between 20 and 70 V for the conventional method, while it remains mostly within ±30 V for the proposed method in the enlarged intervals. This improved balancing is associated with the proposed capacitor-voltage-based selection of redundant switching combinations. These results indicate better neutral-point voltage regulation with the proposed method under the investigated parameter uncertainties and stochastic wind variations.

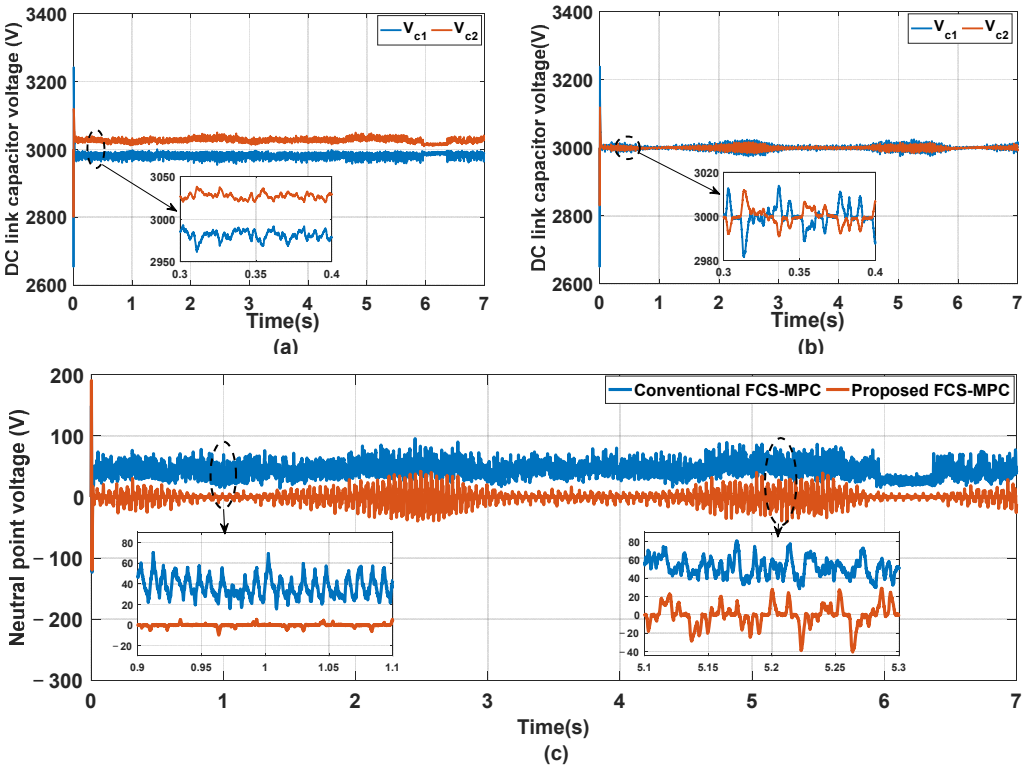


Figure 22. DC-bus capacitor voltage: (**a**) Conventional FCS-MPC, (**b**) proposed FCS-MPC; (**c**) neutral point voltage.

Figure 23 illustrates the quality of the power injected into the grid. The current maintains a sinusoidal waveform and remains in phase with the grid voltage. However, the proposed method achieves better performance, with a THD of 0.99% for a fundamental component of 1841. In comparison, the conventional method shows a THD of 2.43% for a fundamental component of 1832. This difference is explained by the ability of the developed method to maintain a better balance of the DC-bus voltage.

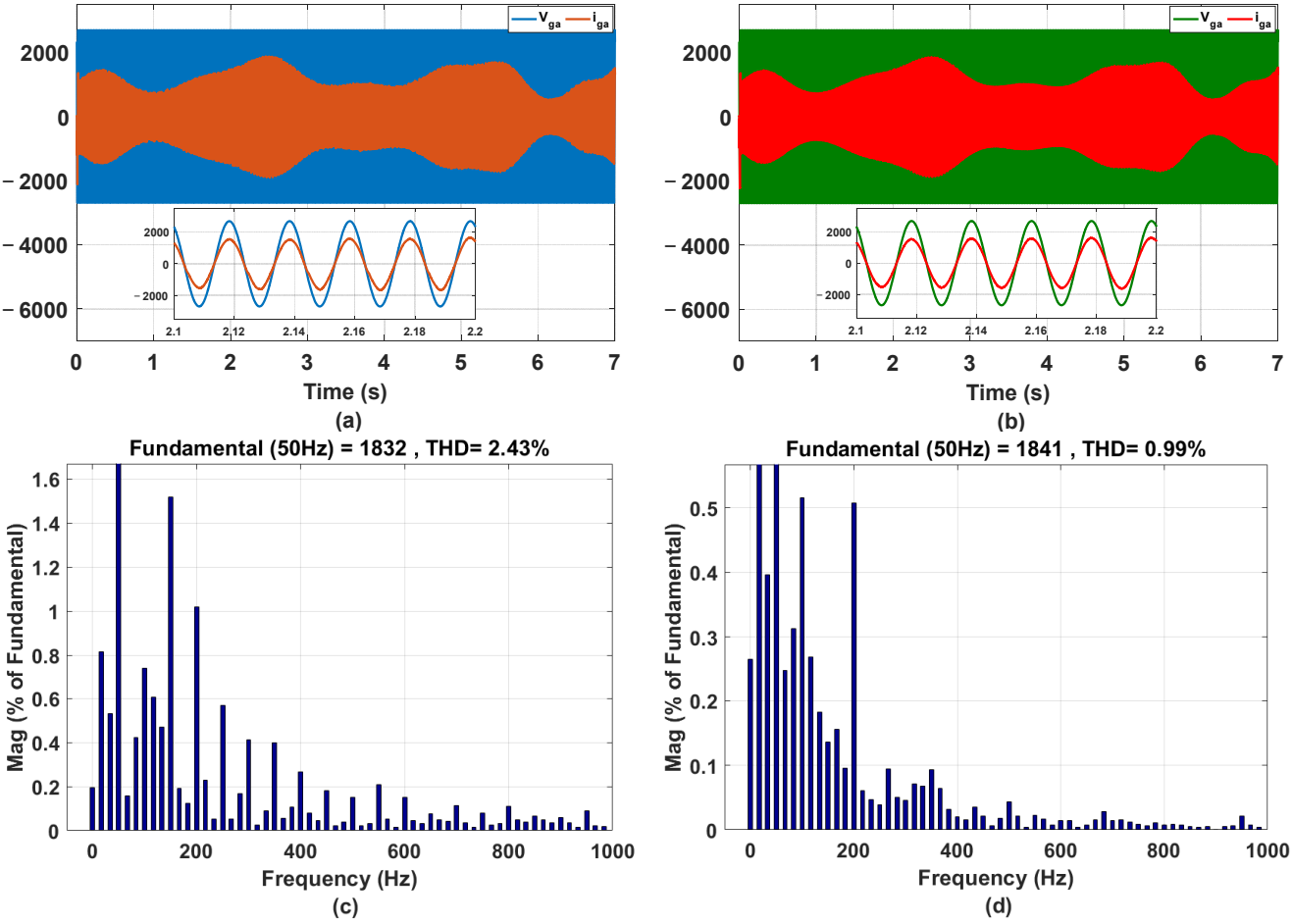


Figure 23. Voltage injected current and grid current THD: (**a**,**c**) Conventional FCS-MPC, (**b**,**d**) proposed FCS-MPC.

To provide a more accurate comparison of the performance of the two control methods, the Integral Absolute Error (IAE) and the Integral Time-weighted Absolute Error (ITAE) were used as evaluation criteria. These performance indices were calculated for each controlled variable of the WECS according to the following expressions:

$$IAE = \int_0^T |e(t)|dt \tag{88}$$

$$ITAE = \int_0^T t.|e(t)|dt \tag{89}$$

where $e(t)$ is the tracking error, and T denotes the simulation time.

The results presented in Tables 10 and 11 show that the proposed method yields lower IAE and ITAE values than the conventional method under both studied scenarios. Under nominal operating conditions, an improvement is observed for all controlled variables. In the presence of parameter uncertainties, the difference between the two methods

becomes significantly more pronounced. For instance, the IAE associated with DC-link neutral-point balancing decreases from 316.30 with the conventional method to 27.39 with the proposed method. Similarly, the errors related to the grid currents $i_{g\alpha}$ and $i_{g\beta}$ are considerably reduced. The same observations can be made using the ITAE values. These results confirm that the proposed method enhances the robustness of the WECS against parameter variations while providing better tracking and neutral-point balancing performance than the conventional method.

Table 10. IAE of two methods in different scenarios.

		Conventional FCS-MPC	**Proposed FCS-MPC**
Scenario 1	IAE_{Ω}(rad)	0.0039	0.0029
	$IAE_{i_{s\alpha}}$(A.s)	156.0029	151.6683
	$IAE_{i_{s\beta}}$(A.s)	98.2649	96.2556
	$IAE_{V_{dc}}$(V. s)	8.0911	7.4851
	$IAE_{\text{neutral point}}$(V.s)	12.1575	5.1377
	$IAE_{i_{g\alpha}}$(A.s)	24.5851	19.1665
	$IAE_{i_{g\beta}}$(A.s)	25.3012	19.0813
Scenario 2	IAE_{Ω}(rad)	0.0052	0.0034
	$IAE_{i_{s\alpha}}$(A.s)	185.9068	159.8271
	$IAE_{i_{s\beta}}$(A.s)	60.4491	58.7251
	$IAE_{V_{dc}}$(V. s)	56.9213	14.9931
	$IAE_{\text{neutral point}}$(V.s)	316.3000	27.3968
	$IAE_{i_{g\alpha}}$(A.s)	262.2899	30.3689
	$IAE_{i_{g\beta}}$(A.s)	296.8757	37.9956

Table 11. ITAE of two methods in different scenarios.

		Conventional FCS-MPC	**Proposed FCS-MPC**
Scenario 1	$ITAE_{\Omega}$(rad. s)	0.0068	0.0043
	$ITAE_{i_{s\alpha}}$(A. s^2)	322.1535	297.3491
	$ITAE_{i_{s\beta}}$(A. s^2)	214.1116	212.9428
	$ITAE_{V_{dc}}$(V. s^2)	16.2503	14.8857
	$ITAE_{\text{neutral point}}$(V. s^2)	30.2494	15.1445
	$ITAE_{i_{g\alpha}}$(A. s^2)	59.9769	43.4956
	$ITAE_{i_{g\beta}}$(A. s^2)	62.2086	43.6028
Scenario 2	$ITAE_{\Omega}$(rad. s)	0.0126	0.0075
	$ITAE_{i_{s\alpha}}$(A. s^2)	560.6524	452.7255
	$ITAE_{i_{s\beta}}$(A. s^2)	210.5726	205.0129
	$ITAE_{V_{dc}}$(V. s^2)	184.7742	40.5959
	$ITAE_{\text{neutral point}}$(V. s^2)	1.0972×10^3	94.1577
	$ITAE_{i_{g\alpha}}$(A. s^2)	896.1704	91.0619
	$ITAE_{i_{g\beta}}$(A. s^2)	980.0140	87.1479

To quantify the optimality loss of the proposed seven-state FCS-MPC compared with the exhaustive 27-state method, two indicators are considered: the Optimality Satisfaction Rate (OSR) and the Mean Optimality Gap. The OSR is defined as:

$$OSR(\%) = 100\frac{N_{eq}}{N} \tag{90}$$

where N_{eq} is the number of sampling instants for which $|f_7^* - f_{27}^*| \leq 10^{-5}$, and N is the total number of samples.

The Mean Optimality Gap is calculated as:

$$\overline{\Delta f} = \frac{1}{N}\sum_{k=1}^{N}(f_7^*(k) - f_{27}^*(k)) \quad (91)$$

where $f_7^*(k)$ and $f_{27}^*(k)$ represent the minimum cost values obtained with 7 and 27 switching states, respectively.

This evaluation is performed under the two operating scenarios considered in this study. For a fair comparison, both algorithms are evaluated using the same system states, inputs, and operating conditions. For the machine-side converter, the cost functions defined in Equations (66) and (72) are considered. For the grid-side converter, the following cost function is used:

$$f = \left[i_{g\alpha}(k+1) - i_{g\alpha}^*(k+1)\right]^2 + \left[i_{g\beta}(k+1) - i_{g\beta}^*(k+1)\right]^2 + 3\sum_{\chi=a,b,c}\sum_{j=1,2}\left[S_{g_{\chi j}} - S_{g_{\chi j}}^{op}\right]^2 \quad (92)$$

The results obtained for both converters under the two operating scenarios are presented in Table 12.

Table 12. Quantitative evaluation of the optimality loss of the proposed FCS-MPC under two operating scenarios.

		OSR (%)	Mean Optimality Gap
Scenario 1	MSC	83.3169	510.9560
	GSC	81.1805	33.2642
Scenario 2	MSC	87.7764	418.6162
	GSC	72.3720	52.3694

As shown in Table 12, the proposed method achieves an Optimality Satisfaction Rate of 83.32% and 81.18% for the machine-side and grid-side converters, respectively, under Scenario 1. Under Scenario 2, the OSR increases to 87.78% for the machine-side converter but decreases to 72.37% for the grid-side converter. The Mean Optimality Gap decreases from 510.96 to 418.62 for the machine-side converter, while it increases from 33.26 to 52.37 for the grid-side converter.

These results indicate that the reduced seven-state search does not always achieve the same minimum cost as the exhaustive 27-state search. Nevertheless, the IAE and ITAE results presented in Tables 10 and 11 show lower tracking and neutral-point balancing errors for the proposed method under both operating scenarios. Although some optimality loss is observed, the results suggest that this loss does not necessarily lead to a degradation in control performance under the tested conditions.

Table 13 provides a comparative evaluation of the proposed method against other approaches from the literature. In [31], the cost function optimization relies on the use of virtual space vectors, improving control performance. However, this method involves a high computational burden, with 33 iterations, and requires the use of an external modulator. In [32], Yang et al. proposed a two-step prediction approach, reducing the number of iterations to nine. However, maintaining a constant switching frequency requires precise adjustment of the switching instants during the second phase, which increases the algorithm's complexity. In [19], Saberi and Rezaie propose predictive current control with adaptive weighting coefficients but also require 27 iterations, thus increasing computational resources. In [20], Mayilsamy et al. introduces a two-step prediction algorithm: the first step identifies the sector with 6 iterations, followed by a second step that performs an additional 6 iterations to determine the optimal combination, for a total of 12 iterations. In [23], Zhang et al. propose a reduced-search strategy based on hexagon and triangle candidate regions to limit the number of evaluated switching states. In contrast, the proposed method requires only seven iterations per sampling period, reducing the number of

evaluated switching combinations. This comparison focuses on computational complexity rather than overall control performance.

Table 13. Comparison between different FCS-MPC methods.

Publication Paper	Candidate Selection Strategy	Evaluated Candidates	Main Distinction
[31]	Virtual space vectors added to the conventional control set	33	Extended control set for neutral-point balancing
[32]	Two-stage prediction using medium and virtual voltage vectors	9	Multiple vectors applied per control cycle for constant switching frequency
[19]	Conventional FCS-MPC with adaptive weighting factors	27	Adaptive cost-function tuning
[23]	Hexagon (HCR) or triangle (TCR) candidate regions	Depends on region	Geometric candidate-region selection
[20]	Two-stage prediction using virtual space vectors and conditional small-vector selection	12	Two successive cost-function evaluations
Proposed FCS-MPC	Quadrant identification using reference-voltage component signs	7	Fixed reduced set of switching combinations selected by quadrant

6. Conclusions

In this study, a sensorless nonlinear control strategy combining ISMC and FCS-MPC is proposed for a PMSG-based WECS employing two 3L-NPC converters. A high-gain observer is developed to estimate grid variables, while an ANN-based MPPT provides the optimal generator speed. The proposed reduced-search FCS-MPC decreases the number of evaluated switching combinations from 27 to 7 per sampling period, reducing the computational burden. The PIL simulation results show satisfactory estimation performance and comparable control performance under nominal conditions. Under parametric uncertainties, the proposed method reduces the IAE of the DC-link voltage by 73.7% and that of the neutral-point voltage by 91.3% compared with conventional FCS-MPC. The grid-current THD is also reduced from 2.43% *to* 0.99%. PIL execution profiling confirms the reduction in computational burden, although real-time feasibility at the adopted sampling period has not been demonstrated.

Future work will focus on online parameter estimation to improve robustness against uncertainties, optimization of the embedded implementation, and experimental real-time validation on a physical WECS platform.

Author Contributions: Conceptualization, A.F., H.A., A.S.A. and M.N.S.; methodology, A.F., H.A., A.S.A., H.A. and H.K.; software, A.F., H.A., K.F. and Y.A.; validation, A.F., A.A.A., H.K. and S.U.; formal analysis, A.F. and H.A.; investigation, A.F., K.F. and Y.A.; writing—original draft preparation, A.F., H.A., K.F. and Y.A.; writing—review and editing, A.S.A., A.A.A., H.K., S.U. and K.F.; visualization, A.F., H.A., M.N.S., H.K. and S.U.; supervision, H.A. and M.N.S.; project administration, H.A. All authors have read and agreed to the published version of the manuscript.

Funding: This research was supported by the Deanship of Scientific Research (DSR) at King Faisal University, Al-Ahsa, Saudi Arabia, under Grant No. KFU266512.

Data Availability Statement: The data are available from the corresponding author upon request.

Conflicts of Interest: The authors declare no conflicts of interest.

References

1. Ullah, A.; Ahmed, M.; Raza, S.A.; Ali, S. A Threshold Approach to Sustainable Development: Nonlinear Relationship between Renewable Energy Consumption, Natural Resource Rent, and Ecological Footprint. *J. Environ. Manag.* **2021**, *295*, 113073. https://doi.org/10.1016/j.jenvman.2021.113073.
2. Oh, B.; Kim, S.; Lee, D. Wind Power Scenario Synthesis with Smoothing Effect Through Spectral Decomposition and Its Application to Flexible Resource Adequacy. *IEEE Trans. Sustain. Energy* **2023**, *14*, 777–789. https://doi.org/10.1109/TSTE.2022.3225272.
3. Blaabjerg, F.; Ma, K. Future on Power Electronics for Wind Turbine Systems. *IEEE J. Emerg. Sel. Top. Power Electron.* **2013**, *1*, 139–152. https://doi.org/10.1109/JESTPE.2013.2275978.
4. Liserre, M.; Cardenas, R.; Molinas, M.; Rodriguez, J. Overview of Multi-MW Wind Turbines and Wind Parks. *IEEE Trans. Ind. Electron.* **2011**, *58*, 1081–1095. https://doi.org/10.1109/TIE.2010.2103910.
5. Zhang, Z.; Wang, F.; Wang, J.; Rodriguez, J.; Kennel, R. Nonlinear Direct Control for Three-Level NPC Back-to-Back Converter PMSG Wind Turbine Systems: Experimental Assessment With FPGA. *IEEE Trans. Ind. Inform.* **2017**, *13*, 1172–1183. https://doi.org/10.1109/TII.2017.2678500.
6. Zhang, Z.; Li, Z.; Kazmierkowski, M.P.; Rodriguez, J.; Kennel, R. Robust Predictive Control of Three-Level NPC Back-to-Back Power Converter PMSG Wind Turbine Systems with Revised Predictions. *IEEE Trans. Power Electron.* **2018**, *33*, 9588–9598. https://doi.org/10.1109/TPEL.2018.2796093.
7. Naik, K.A.; Gupta, C.P.; Fernandez, E. Design and Implementation of Interval Type-2 Fuzzy Logic-PI Based Adaptive Controller for DFIG Based Wind Energy System. *Int. J. Electr. Power Energy Syst.* **2020**, *115*, 105468. https://doi.org/10.1016/j.ijepes.2019.105468.
8. El Mourabit, Y.; Derouich, A.; El Ghzizal, A.; El Ouanjli, N.; Zamzoum, O. Nonlinear Backstepping Control for PMSG Wind Turbine Used on the Real Wind Profile of the Dakhla-Morocco City. *Int. Trans. Electr. Energy Syst.* **2020**, *30*, e12297. https://doi.org/10.1002/2050-7038.12297.
9. Fathelkhair, A.; Abouobaida, H.; Mchaouar, Y.; Abouelmahjoub, Y.; Oualifi, K.; Akli, H. Sensorless Nonlinear Control Based on Integral Backstepping Technique for PMSG- Based Wind Energy Conversion System. *IFAC-PapersOnLine* **2024**, *58*, 448–453. https://doi.org/10.1016/j.ifacol.2024.07.523.
10. Lasheen, A.; Elnaggar, M.; Yassin, H. Adaptive Control Design and Implementation for Collective Pitch in Wind Energy Conversion Systems. *ISA Trans.* **2020**, *102*, 251–263. https://doi.org/10.1016/j.isatra.2019.11.019.
11. Osman, A.M.; Alsokhiry, F. Sliding Mode Control for Grid Integration of Wind Power System Based on Direct Drive PMSG. *IEEE Access* **2022**, *10*, 26567–26579. https://doi.org/10.1109/ACCESS.2022.3157311.
12. Douara, B.O.; Kouzou, A.; Hafaifa, A.; Rodriguez, J.; Abdelrahem, M. An Enhanced Second-Order Terminal Sliding Mode Control Based on the Super-Twisting Algorithm Applied to a Five-Phase Permanent Magnet Synchronous Generator for a Grid-Connected Wind Energy Conversion System. *Energies* **2025**, *18*, 355. https://doi.org/10.3390/en18020355.
13. Nguyen, H.T.; Al-Sumaiti, A.S.; Vu, V.-P.; Al-Durra, A.; Do, T.D. Optimal Power Tracking of PMSG Based Wind Energy Conversion Systems by Constrained Direct Control with Fast Convergence Rates. *Int. J. Electr. Power Energy Syst.* **2020**, *118*, 105807. https://doi.org/10.1016/j.ijepes.2019.105807.
14. Hamid, H.B.A.; Hassan, J.N.A.; Ali, G.H.; Ma, T.; Ko, C.; Khan, H.; Mohammed, O.A.A.; Shahid, A. Improved Finite Control Set Model Predictive Current Control Design for Variable-Speed Wind-Energy Conversion System Connected to the Grid via an LCL Filter. *Sci. Rep.* **2026**, *16*, 19106. https://doi.org/10.1038/s41598-026-50228-4.
15. Wang, H.; Chen, X.; Liu, Y.; Su, M.; Feng, W.; Yu, W. Model Predictive Control of Three-Phase Voltage-Source Converters with Improved Tracking Performance. *ISA Trans.* **2023**, *133*, 424–434. https://doi.org/10.1016/j.isatra.2022.07.012.
16. Rodriguez, J.; Kazmierkowski, M.P.; Espinoza, J.R.; Zanchetta, P.; Abu-Rub, H.; Young, H.A.; Rojas, C.A. State of the Art of Finite Control Set Model Predictive Control in Power Electronics. *IEEE Trans. Ind. Inform.* **2013**, *9*, 1003–1016. https://doi.org/10.1109/TII.2012.2221469.
17. Babaghorbani, B.; Beheshti, M.T.; Talebi, H.A. A Lyapunov-Based Model Predictive Control Strategy in a Permanent Magnet Synchronous Generator Wind Turbine. *Int. J. Electr. Power Energy Syst.* **2021**, *130*, 106972. https://doi.org/10.1016/j.ijepes.2021.106972.
18. Nouraldin, N.A.; Chebaani, M.; Számel, L.; Abdelwahab, S.A.M.; Abdellatif, W.S.E. Experimental Investigation of Predictive Control for PMSM-Based Wind Turbine Generation System. *Comput. Electr. Eng.* **2024**, *119*, 109554. https://doi.org/10.1016/j.compeleceng.2024.109554.
19. Saberi, S.; Rezaie, B. Robust Adaptive Direct Speed Control of PMSG-Based Airborne Wind Energy System Using FCS-MPC Method. *ISA Trans.* **2022**, *131*, 43–60. https://doi.org/10.1016/j.isatra.2022.04.035.

20. Mayilsamy, G.; Lee, S.R.; Joo, Y.H. An Improved Model Predictive Control of Back-to-Back Three-Level NPC Converters with Virtual Space Vectors for High Power PMSG-Based Wind Energy Conversion Systems. *ISA Trans.* **2023**, *143*, 503–524. https://doi.org/10.1016/j.isatra.2023.09.033.
21. Fathelkhair, A.; Abouobaida, H.; Mchaouar, Y.; Abouelmahjoub, Y.; Elmesouli, D.; Oualifi, K. Nonlinear Control for a Single Phase Grid Connected Wind Energy System. In *Automatic Control and Emerging Technologies*; El Fadil, H., Zhang, W., Eds.; Lecture Notes in Electrical Engineering; Springer Nature: Singapore, 2024; Volume 1141, pp. 334–347.
22. Watil, A.; El Magri, A.; Raihani, A.; Lajouad, R.; Giri, F. An Adaptive Nonlinear Observer for Sensorless Wind Energy Conversion System with PMSG. *Control Eng. Pract.* **2020**, *98*, 104356. https://doi.org/10.1016/j.conengprac.2020.104356.
23. Zhang, Z.; Hackl, C.M.; Kennel, R. Computationally Efficient DMPC for Three-Level NPC Back-to-Back Converters in Wind Turbine Systems With PMSG. *IEEE Trans. Power Electron.* **2017**, *32*, 8018–8034. https://doi.org/10.1109/TPEL.2016.2637081.
24. Watil, A.; El Magri, A.; Raihani, A.; Lajouad, R.; Giri, F. Multi-Objective Output Feedback Control Strategy for a Variable Speed Wind Energy Conversion System. *Int. J. Electr. Power Energy Syst.* **2020**, *121*, 106081. https://doi.org/10.1016/j.ijepes.2020.106081.
25. Fathelkhair, A.; Abouobaida, H.; Mchaouar, Y.; Abouelmahjoub, Y.; Oualifi, K.; Guerrero, J.M. Sensorless Nonlinear Control of Permanent Magnet Synchronous Generator Based Wind Energy Conversion Systems. *Electr. Eng.* **2025**, *107*, 9921–9948. https://doi.org/10.1007/s00202-025-03008-8.
26. Yang, Y.; Wen, H.; Fan, M.; Xie, M.; Chen, R.; Wang, Y. A Constant Switching Frequency Model Predictive Control Without Weighting Factors for T-Type Single-Phase Three-Level Inverters. *IEEE Trans. Ind. Electron.* **2019**, *66*, 5153–5164. https://doi.org/10.1109/TIE.2018.2868290.
27. El Myasse, I.; El Magri, A.; Watil, A.; Ashfaq, S.; Kissaoui, M.; Lajouad, R. Improvement of Real-Time State Estimation Performance in HVDC Systems Using an Adaptive Nonlinear Observer. *IFAC J. Syst. Control* **2024**, *27*, 100244. https://doi.org/10.1016/j.ifacsc.2024.100244.
28. Taghinezhad, J.; Sheidaei, S. Prediction of Operating Parameters and Output Power of Ducted Wind Turbine Using Artificial Neural Networks. *Energy Rep.* **2022**, *8*, 3085–3095. https://doi.org/10.1016/j.egyr.2022.02.065.
29. Ocampo, I.; López, R.R.; Camacho-León, S.; Nerguizian, V.; Stiharu, I. Comparative Evaluation of Artificial Neural Networks and Data Analysis in Predicting Liposome Size in a Periodic Disturbance Micromixer. *Micromachines* **2021**, *12*, 1164. https://doi.org/10.3390/mi12101164.
30. Majout, B.; Bossoufi, B.; Karim, M.; Skruch, P.; Mobayen, S.; Mourabit, Y.E.; Laggoun, Z.E.Z. Artificial Neural Network-Based Direct Power Control to Enhance the Performance of a PMSG-Wind Energy Conversion System under Real Wind Speed and Parameter Uncertainties: An Experimental Validation. *Energy Rep.* **2024**, *11*, 4356–4378.
31. Alhosaini, W.; Wu, Y.; Zhao, Y. An Enhanced Model Predictive Control Using Virtual Space Vectors for Grid-Connected Three-Level Neutral-Point Clamped Inverters. *IEEE Trans. Energy Convers.* **2019**, *34*, 1963–1972. https://doi.org/10.1109/TEC.2019.2923370.
32. Yang, Y.; Wen, H.; Chen, R.; Fan, M.; Zhang, X.; Norambuena, M.; Rodriguez, J. An Efficient Model Predictive Control Using Virtual Voltage Vectors for Three-Phase Three-Level Converters With Constant Switching Frequency. *IEEE Trans. Ind. Electron.* **2022**, *69*, 3998–4009. https://doi.org/10.1109/TIE.2021.3075890.

Disclaimer/Publisher's Note: The statements, opinions and data contained in all publications are solely those of the individual author(s) and contributor(s) and not of MDPI and/or the editor(s). MDPI and/or the editor(s) disclaim responsibility for any injury to people or property resulting from any ideas, methods, instructions or products referred to in the content.